INTERNATIONAL JOURNAL FOR NUMERICAL METHODS IN FLUIDS, VOL. 26, 369–401 (1998)

GRID CONVERGENCE STUDIES FOR THE PREDICTION OF HURRICANE STORM SURGE

C. A. BLAIN[1]* J. J. WESTERINK[2] AND R. A. LUETTICH JR.[3]

[1] *Naval Research Laboratory, Code 7322, Stennis Space Center, MS 39529, U.S.A.*
[2] *Department of Civil Engineering and Geological Sciences, University of Notre Dame, Notre Dame, IN 46556, U.S.A.*
[3] *University of North Carolina at Chapel Hill, Institute of Marine Sciences, 3431 Arendell St., Morehead City, NC 28557, U.S.A.*

SUMMARY

The focus of this paper is a systematic determination of the relationship between grid resolution and errors associated with computations of hurricane storm surge. A grid structure is sought that provides the spatial resolution necessary to capture pertinent storm surge physics and does not overdiscretize. A set of numerical experiments simulating storm surge generation over 14 grid discretizations of idealized domains examines the influence of grid spacing, shoreline detail, coastline resolution and characteristics of the meteorological forcing on storm surge computations. Errors associated with a given grid are estimated using a Richardson-based error estimator. Analysis of the magnitude and location of estimated errors indicates that underresolution on the continental shelf leads to significant overprediction of the primary storm surge. In deeper waters, underresolution causes smearing or damping of the inverted barometer forcing function, which in turn results in underprediction of the surge elevation. In order to maintain a specified error level throughout the duration of the storm, the highest grid resolution is required on the continental shelf and particularly in nearshore areas. The disparity of discretization requirements between deep waters and coastal regions is best met using a graded grid. Application of the graded gridding strategy to the hindcast of Hurricane Camille reinforces the necessity of using a grid that has high levels of resolution in nearshore regions and areas of complex coastal geometry. © 1998 John Wiley & Sons, Ltd.

Int. J. Numer. Meth. Fluids, **26**: 369–401 (1998).

KEY WORDS: storm surge; shallow water model; grid convergence; coastal ocean

1. INTRODUCTION

A major shortcoming in coastal ocean modelling work is the lack of adequate studies to evaluate convergence with regard to grid spacing and grid structure. The degree of spatial resolution provided by a grid of discrete points is pivotal to obtaining accurate computed model solutions. Truncation errors, and the associated amplitude and phase propagation characteristics, as well as aliasing of energy near the resolution limit all affect the computed water body response and depend on grid spacing and structure. Consequently, in assessing hydrodynamic model performance, any errors resulting from inadequate grid resolution must be identified and reduced to a defined acceptable level.

Correspondence to: C. A. Blain, Naval Research Laboratory, Code 7322, Stennis Space Center, MS 39529, U.S.A.
Contract grant sponsor: US Army Engineer Waterways Experiment Station; Contract grant number: DACW-39-90-K-0021; Coantract grant number: DACW-39-95-K-0011
Contract grant sponsor: National Science Foundation; Contract grant number: OCE-9116448

CCC 0271–2091/98/040369–33 $17.50

Received 15 April 1996
Revised 27 January 1997

Too often, model grids are constructed using subjective criteria and their discretizations are based on computational constraints. Only recently have there been efforts to establish the level to which the computed physics has converged by doing systematic grid convergence studies for tidal, wind-driven and large-scale baroclinic circulation.[1–13] For the majority of storm surge model applications the importance of adequate grid resolution and the advantage of spatially varying resolution throughout the computational domain are recognized.[14–22] However, there is little evidence of rigorous studies assessing error trends associated with inadequate spatial resolution and the influence of grid structure on storm surge prediction.

The focus of this paper is a systematic determination of the relationship between grid resolution and predictions of primary hurricane storm surge. A grid structure is sought that provides the spatial resolution necessary to capture pertinent storm surge physics and does not overdiscretize. This is particularly important if model efficiency is to be preserved when using large computational domains, as suggested by the results of the domain size sensitivity study of Blain *et al.*[23]

To evaluate grid convergence, the magnitude and location of errors in the predicted storm surge associated with discrete representations of the domain are calculated. Errors are quantified using a Richardson-based error estimator.[24] Error estimates for a given grid are obtained using two discrete solutions having different spatial resolutions. The error analysis conducted here leads to an assessment of model performance relative to the grid discretization.

A set of numerical experiments simulates storm surge generation over a series of grids discretizing two idealized domains. Results of these experiments illuminate the influence of grid spacing, shoreline detail, coastline resolution and characteristics of the meteorological forcing on hurricane storm surge calculations. Both extreme and normalized errors in the storm surge computed for each grid discretization are related to distance from the coast, bathymetry and grid spacing. This analysis suggests that an appropriate grid structure for modelling hurricane storm surge generation provides the highest level of grid resolution on the shelf and in the vicinity of the coast. This gridding strategy is then applied to the simulation of storm surge generated by Hurricane Camille over a model domain which incorporates the western North Atlantic Ocean, Gulf of Mexico and Caribbean Sea. Note that these results are not necessarily applicable to all wave propagation. In particular, Luettich and Westerink[13] and Westerink *et al.*[11] have demonstrated that additional resolution at the shelf break and slope is necessary to achieve improved accuracy for tidal computations.

2. HYDRODYNAMIC MODEL DESCRIPTION

The hydrodynamic computations were performed using ADCIRC-2DDI, the depth-integrated option of a set of two- and three-dimensional fully non-linear hydrodynamic codes named ADCIRC.[25] ADCIRC-2DDI uses the vertically averaged equations of mass and momentum conservation, subject to the hydrostatic pressure approximation. For the applications in this paper the standard quadratic parametrization for bottom stress is used and the baroclinic terms, the finite amplitude terms and the lateral diffusion/dispersion terms are all neglected, leading to the following set of conservation statements in primitive form expressed in a spherical co-ordinate system:[26]

$$\frac{\partial \zeta}{\partial t} + \frac{1}{R\cos\phi}\left(\frac{\partial (Uh)}{\partial \lambda} + \frac{\partial (Vh\cos\phi)}{\partial \phi}\right) = 0, \tag{1}$$

$$\frac{\partial U}{\partial t} + \frac{1}{R\cos\phi}U\frac{\partial U}{\partial \lambda} + \frac{1}{R}V\frac{\partial U}{\partial \phi} - \left(\frac{\tan\phi}{R}U + f\right)V = -\frac{1}{R\cos\phi}\frac{\partial}{\partial \lambda}\left(\frac{p_s}{\rho_0} + g\zeta\right) + \frac{\tau_{s\lambda}}{\rho_0 h}\tau_* U, \tag{2}$$

$$\frac{\partial V}{\partial t} + \frac{1}{R\cos\phi}U\frac{\partial V}{\partial \lambda} + \frac{1}{R}V\frac{\partial V}{\partial \phi} + \left(\frac{\tan\phi}{R}U + f\right)U = -\frac{1}{R}\frac{\partial}{\partial \phi}\left(\frac{p_s}{\rho_0} + g\zeta\right) + \frac{\tau_{s\phi}}{\rho_0 h} - \tau_* V. \tag{3}$$

Here t represents time, λ and ϕ are degrees longitude (east of Greenwich positive) and degrees latitude (north of the equator positive) respectively, ζ is the free surface elevation relative to the geoid, U and V are the depth-averaged horizontal velocities, R is the radius of the Earth, h is the bathymetric depth relative to the geoid, $f = 2\Omega \sin\phi$ is the Coriolis parameter, Ω is the angular speed of the Earth, p_s is the atmospheric pressure at the free surface, g is the acceleration due to gravity, ρ_0 is the reference density of water, $\tau_{s\lambda}$ and $\tau_{s\phi}$ are the applied free surface stresses and τ_* is given by the expression $C_f(U^2 + V^2)^{1/2}/h$, where C_f is the bottom friction coefficient.

Equations (1)–(3) are reformulated into a generalized wave continuity equation (GWCE) and are subsequently discretized using the finite element (FE) method.[27–29] ADCIRC-2DDI has been implemented using linear, triangular finite elements. The details of ADCIRC-2DDI are described by Luettich *et al.*[25] and Kolar *et al.*[26,30] It is noted that shoreline wetting and/or drying were not accounted for in the calculations presented in this paper.

Computations of hurricane wind stress and pressure fields are carried out using a modified form of the HURWIN wind model.[31] An exponential pressure law is used in the HURWIN model to generate a circularly symmetric pressure field situated at the low-pressure centre of the storm:

$$p_s = p_{eye} + \Delta p e^{-(R_s/r)}. \tag{4}$$

Here p_s is the spatially and temporally varying pressure field, p_{eye} is the pressure at the centre or eye of the storm, $\Delta p = \bar{p} - p_{eye}$ is the pressure anomaly, with $\bar{p}$ taken as an average background pressure, and r is the radial distance outward from the eye of the storm. The scale radius R_s, assumed equivalent to the radius to maximum wind, R_{max}, is computed from an approximation of a nomograph relating R_{max} to the maximum wind speed and the pressure anomaly.[32] Wind speed computed by the HURWIN model is obtained by solving the equations of horizontal motion which have been vertically averaged through the planetary boundary layer. These wind speeds are then converted to surface wind stresses using a quadratic drag law proposed by Garratt[33] and are subsequently used as forcing for the hydrodynamic model.

3. SYSTEMATIC GRID CONVERGENCE STUDIES

3.1. Domain and grid descriptions

An investigation into the grid resolution requirements for accurate prediction of hurricane storm surge is conducted using two idealized domains and a series of regular and variably graded grids. The first domain consists of a rectangle of dimension 2500 km (northern and southern sides) by 3000 km (western and eastern sides) and approximates the areal extent of the large domain used by Blain *et al.*[23] to study hurricane storm surge. Specifically, the rectangular domain idealizes the continental margin waters in the Atlantic Ocean off the eastern shore of the United States. Note that this idealized domain does not exhibit the resonant characteristics observed in the Gulf of Mexico or Caribbean Sea. The western boundary of the rectangular domain represents a straight coastline, while the remaining boundaries extend into the open ocean. A representative bathymetric profile, shown in Figure 1, is synthesized from ocean depth cross-sections recorded off the coasts of Virginia and Florida in the western North Atlantic Ocean and is expressed mathematically as

$$d = \begin{cases} |x - x_{coast}|0{\cdot}0013, & x \le x_{shelf\ break}, \\ (|x - x_{coast}| - 100{\cdot}0)\ 0{\cdot}025 + 130{\cdot}0, & x_{shelf\ break} < x \le x_{toe\ of\ slope}, \\ (|x - x_{coast}| - 215{\cdot}0)\ 0{\cdot}002 + 3000{\cdot}0, & x_{toe\ of\ slope} < x \le x_{toe\ of\ rise}, \\ 7000{\cdot}0, & x > x_{toe\ of\ rise}, \end{cases} \tag{5}$$

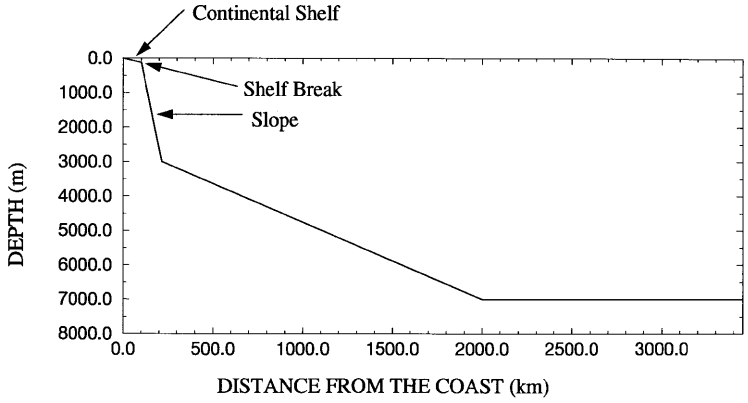

Figure 1. Bathymetric profile in north–south orientation for rectangular domain grids

where d is the bathymetry in metres and x is the distance away from the shoreline in kilometres. This profile remains uniform in a north–south orientation and defines the bathymetric function for all grids.

The second domain is a variation of the rectangular domain and incorporates a sinusoidally varying coastline with a wavelength of 100 km and an amplitude of 30 km. This domain is intended to portray in an idealized way the often irregular profile of actual coastlines. A bathymetric profile similar to that used for the rectangular domain is specified from the shoreline. The north–south bathymetric variability is attenuated away from the coastline such that effects of the coastline variation on the bathymetric profile remain on the continental shelf.

Fourteen discretizations form the basis of this grid convergence study. For the first rectangular domain, three uniform grids designated G50, G25 and G12·5 have regular nodal spacings of 50, 25 and 12·5 km respectively. Two variably graded grids, VG1 and VG2, have nodal spacings ranging between 12·5 and 50 km. Figure 2 depicts enlargements of the continental shelf and slope portion of the discretization for both variably graded grids. For grid VG1 (Figure 2(a)) the grid spacing is 12·5 km from the shoreline to 25 km offshore, 25 km over the remainder of the continental shelf and 50 cm elsewhere. For VG2 (Figure 2(b)) the grid size is 12·5 km over the entire continental shelf, shelf break and portions of the continental slope out to a depth of approximately 1000 m; the spacing over the remainder of the deep ocean increases rapidly from 12·5 to 50 km. Two additional grids, CVG1 and CVG2, are fourfold refinements (twice the resolution in each direction) of grids VG1 and VG2 respectively.

For the sinusoidal coastline domain, three uniform grids have spacings of 50, 25 and 12·5 km respectively and are designated grids G50_C5, G25_C9 and G12·5_C17. Owing to their different levels of spatial discretization, each of the grids represent the coastline somewhat uniquely as shown in Figure 3. Grid G50_C5 resolves every sinusoid in the coastline with five nodes (Figure 3(a)). Clearly the shoreline is poorly represented by this coarse representation. Grids G25_C9 and G12·5_C17 use nine and 17 nodes per wavelength of the sinusoid respectively as seen in Figures 3(b) and 3(c) and result in progressively better representations of the shoreline. Two variably graded grids, VG1_C17 and VG2_C17, whose shelf and slope discretizations are shown in Figure 4, have nodal spacings between 12·5 and 50 km and are arranged similarly to grids VG1 and VG2. The near-coastal zone in each of these grids is resolved with a grid spacing of 12·5 km and the shoreline itself is resolved with 17 nodes per sinusoid. Finally, two additional grids, CVG1_C17 and CVG2_C17, represent fourfold spatial refinements (a factor of two in each direction) of grids VG1_C17 and

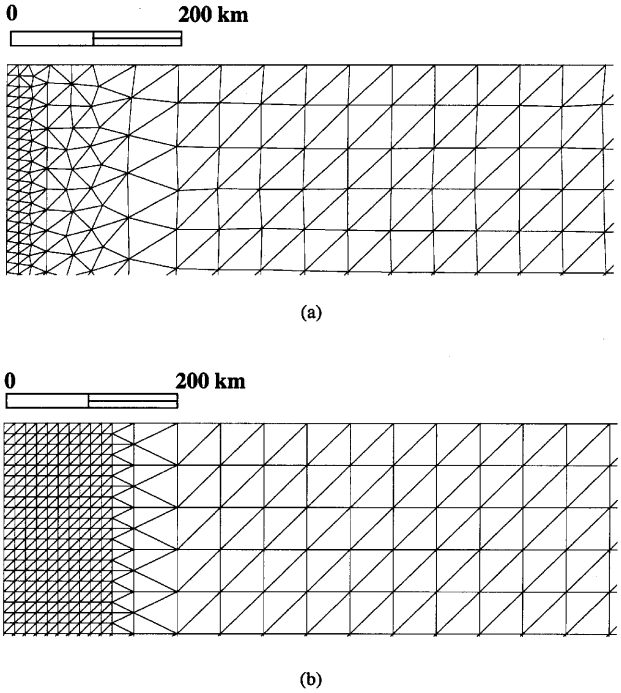

Figure 2. Enlargements of portions of graded discretizations for grids (a) VG1 and (b) VG2

VG2_C17 respectively. These latter two grids maintain an identical representation of the shoreline as grids VG1_C17 and VG2_C17 (i.e. 17 nodes per sinusoid).

Table I summarizes the distinguishing features of each of the 14 grids used in the grid convergence study.

3.2. Hurricane forcing and storm surge computations

Four synthetic hurricanes, H11, H12, H13 and H31, serve as the meteorological forcing for all cases. Two hurricane paths are considered, one perpendicular to the coast (indicated by first index equal to 1, i.e. H11, H12, H13) and one approaching within 60 km parallel to the shoreline (first index equal to 3, i.e. H31). Combinations of two constant storm scales, $R_s = 30$ and 60 km, and two constant storm velocities, 15 and 25 km h^{-1} defined as the forward speed of the eye, are considered in defining the synthetic hurricanes (indicated by the second index equal to 1, 2 or 3). All synthetic hurricanes have a constant pressure deficit of 80 mbar and no background surface winds are applied. The hurricane parameters used here are based on averages of the parameters associated with six historical hurricanes (Kate, Eloise, Elena, Hugo, Danny and Camille) and the parameters utilized in the work of Bunpapong *et al.*[34] Table II summarizes the characteristics of the four synthetic hurricanes.

In the simulations of storm surge, wind stress and pressure forcing from the synthetic hurricanes are applied on the interior of the domain and tidal forcing is neglected both on the interior and at the open ocean boundaries. Additionally, an inverted barometer condition consistent with the atmospheric pressure field is specified at the open ocean boundaries of the domain.[23] For this

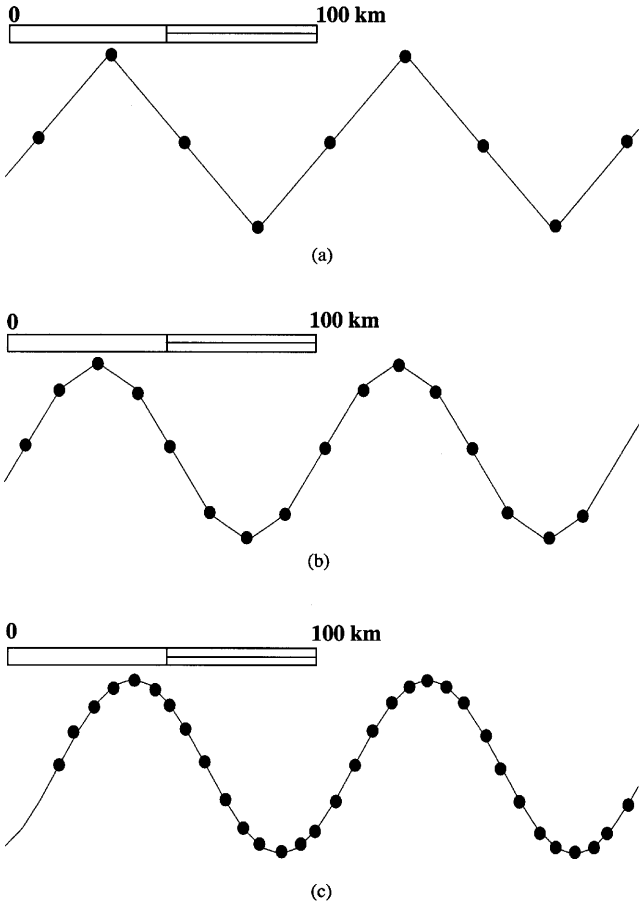

Figure 3. Discretizations of sinusoidal coastline variation using (a) five, (b) nine and (c) 17 points per wavelength

series of simulations, hydrodynamic model parameters are identical so that comparisons between computations for the various storms over each grid discretization are possible. The bottom friction coefficient is constant and equal to 0·003 and the GWCE parameter τ_0 has units of s^{-1} and is set equal to 0·001.[29,30]

Simulations are spun up from homogeneous initial conditions. A hyperbolic ramp function of 1 day length is applied to the wind and pressure forcing as well as the inverted barometer boundary condition. The hurricane wind and pressure fields are held constant during the first 6 h of the ramping period. Thereafter, storm surge computations use time-varying wind and pressure fields. A constant time step of either 22·5 or 45 s is used for all simulations. Selection of the time step is such that Courant numbers based on the wave celerity in deep water are always well below one (typically below 0·24), while in the shallowest waters they are always below 0·02. Consequently the time discretization remains highly resolved and satisfies the Courant number requirements for both stability (since some non-linear terms are explicitly treated) and accuracy (to avoid a folded dispersion relationship).

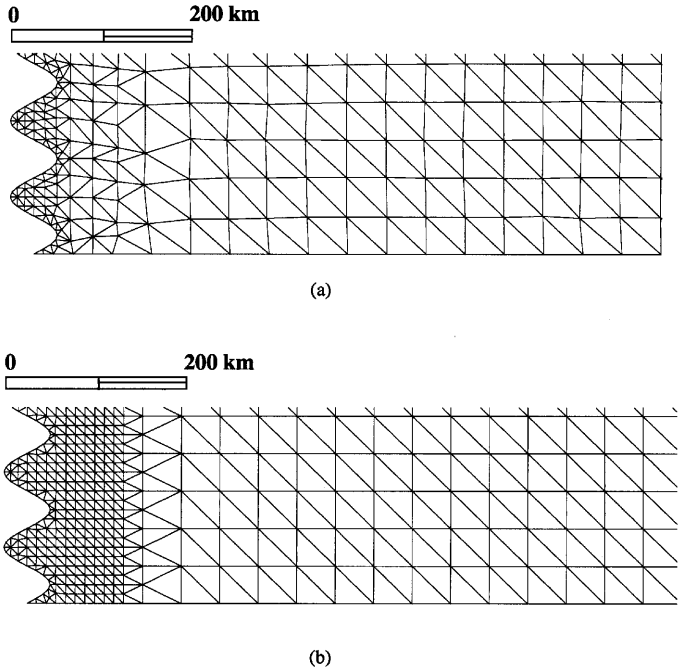

Figure 4. Enlargements of portions of graded discretizations for grids (a) VG1_C17 and (b) VG2_C17

3.3. Grid comparisons

The goal of this paper is to assess the performance of the defined grids in computing storm surge for the two idealized domains and the various sets of storm parameters specified in the previous two subsections. Initially, comparisons are made between solutions obtained over grids G50, G25, G12·5, VG1, VG2, CVG1 and CVG2 for the rectangular domain. Subsequently, solutions computed for the

Table I. Characteristics of rectangular domain grid discretizations

Name	Coastline		Grid		Number of nodes
	Type	Representation	Structure	Spacing (km)	
G50	Straight	—	Regular	50	3111
G25	Straight	—	Regular	25	12221
G12·5	Straight	—	Regular	12·5	48441
VG1	Straight	—	Graded	12·5–50	4014
VG2	Straight	—	Graded	12·5–50	5639
CVG1	Straight	—	Graded	6·2–25	15647
CVG2	Straight	—	Graded	6·2–25	22137
G50_C5	Sinusoidal	5 pts	Regular	50	3171
G25_C9	Sinusoidal	9 pts	Regular	25	12401
G12·5_C17	Sinusoidal	17 pts	Regular	12·5	49040
VG1_C17	Sinusoidal	17 pts	Graded	12·5–50	4374
VG2_C17	Sinusoidal	17 pts	Graded	12·5–50	5910
CVG1_C17	Sinusoidal	17 pts	Graded	6·2–25	16847
CVG2_C17	Sinusoidal	17 pts	Graded	6·2–25	22981

Table II. Characteristics of synthetic hurricanes

Hurricane name	Storm scale (km)	Forward speed ($km\,h^{-1}$)	Hurricane path (relative to coast)	Simulation period (days)	Time of landfall (h)
H11	30	15	Perpendicular	8·75	192
H12	60	15	Perpendicular	8.75	192
H13	30	25	Perpendicular	6.00	126
H31	30	15	Parallel	20·50	—

domain with the sinusoidally varying coastline using grids G50_C5, G25_C9, C12·5_C17, VG1_C17, VG2_C17, CVG1_C17 and CVG2_C17 are compared. The objective of this error analysis is to determine the magnitude and location of errors in the predicted storm surge throughout the computational domain. A systematic examination of these errors in relation to the grid discretization highlights general resolution requirements which can be used to construct grids which accurately represent storm surge generation in the coastal ocean without overdiscretizing the domain.

The errors for each grid relative to a doubly refined grid solution are estimated by computing a Richardson-based error estimator.[24] The Richardson-based error estimates the leading-order truncation error using Richardson extrapolation. By comparing the difference between solutions obtained with a coarse grid and a fine grid, an estimate of the error associated with each grid is made. For the coarse grid the Richardson-based error estimate E is computed as

$$E^{\mathrm{C}}_{\underline{\text{coarse}}-\text{fine}} = \frac{r^p}{r_p - 1}\varepsilon, \tag{6}$$

where $r = \Delta x_{\text{coarse}}/\Delta x_{\text{fine}}$ is the refinement index, Δx_{coarse} is specified as the coarse grid spacing, Δx_{fine} is equal to the fine grid spacing, p is the formal order of the spatial discretization and ε is a measure of the difference in the solutions for the coarse and fine grids. For the fine grid, E is computed as[24]

$$E^{\mathrm{F}}_{\text{coarse}-\underline{\text{fine}}} = \frac{1}{r_p - 1}\varepsilon. \tag{7}$$

Since all grid comparisons are based on a fourfold increase in nodal density (grid spacing is halved in each direction), $r = 2$. The GWCE-based finite element solution with linear triangular elements is formally second-order-accurate in space and therefore $p = 2$. Note that time discretization errors were analysed and determined to be negligible for all grids considered for each domain and set of storms. Thus the computed values of the estimate E can be almost entirely attributed to inadequate spatial discretization. However, observed convergence rates will typically still be less than the formal rate $r = 2$ owing to factors such as competition between truncation terms, non-linear effects or not having achieved the asymptotic range.[35]

Forms of the differences in the solutions, ε, computed over each grid as a function of time include extreme overprediction (positive) and underprediction (negative) errors in the storm surge. The extreme overprediction error is represented as ${}^{\mathrm{o}}E^{\mathrm{C}}_{\underline{\text{coarse}}-\text{fine}}$ or ${}^{\mathrm{o}}E^{\mathrm{F}}_{\text{coarse}-\underline{\text{fine}}}$, where

$${}^{\mathrm{o}}\varepsilon = \max(f_{\text{coarse grid}} - f_{\text{fine grid}}) \tag{8}$$

and $f_{\text{coarse grid}}$ and $f_{\text{fine grid}}$ represent the coarse and fine grid computed surface elevations as a function of space and time. The extreme underprediction errors ${}^{\mathrm{u}}E^{\mathrm{C}}_{\underline{\text{coarse}}-\text{fine}}$ and ${}^{\mathrm{u}}E^{\mathrm{F}}_{\text{coarse}-\underline{\text{fine}}}$ utilize the minimum difference between the coarse grid and fine solutions as a function of time so that

$${}^{\mathrm{u}}\varepsilon = \min(f_{\text{coarse grid}} - f_{\text{fine grid}}). \tag{9}$$

Table III. Richardson-based error estimators for grids using (a) rectangular domain and (b) a rectangular domain with a sinusoidal coastline

Grid (a)	Richardson-based error estimator	Grid (b)	Richardson-based error estimator
G50	$E^{\mathrm{C}}_{\underline{\mathrm{G50}}-\mathrm{G25}}$	G50_C5	$E^{\mathrm{C}}_{\underline{\mathrm{G50\_C5}}-\mathrm{G25\_C9}}$
G25	$E^{\mathrm{F}}_{\mathrm{G50}-\underline{\mathrm{G25}}}$, $E^{\mathrm{C}}_{\underline{\mathrm{G25}}-\mathrm{G12{\cdot}5}}$	G25_C9	$E^{\mathrm{F}}_{\mathrm{G50\_C5}-\underline{\mathrm{G25\_C9}}}$, $E^{\mathrm{C}}_{\underline{\mathrm{G25\_C9}}-\mathrm{G12{\cdot}5\_C17}}$
G12·5	$E^{\mathrm{F}}_{\mathrm{G25}-\underline{\mathrm{G12{\cdot}5}}}$	G12·5_C17	$E^{\mathrm{F}}_{\mathrm{G25\_C9}-\underline{\mathrm{G12{\cdot}5\_C17}}}$
VG1	$E^{\mathrm{C}}_{\underline{\mathrm{VG1}}-\mathrm{CVG1}}$	VG1_C17	$E^{\mathrm{C}}_{\underline{\mathrm{VG1\_C17}}-\mathrm{CVG1\_C17}}$
VG2	$E^{\mathrm{C}}_{\underline{\mathrm{VG2}}-\mathrm{CVG2}}$	VG2_C17	$E^{\mathrm{C}}_{\underline{\mathrm{VG2\_C17}}-\mathrm{CVG2\_C17}}$

The normalized overprediction and underprediction errors ${}^{\mathrm{o/n}}E^{\mathrm{C}}_{\underline{\mathrm{coarse}}-\mathrm{fine}}$, ${}^{\mathrm{o/n}}E^{\mathrm{F}}_{\mathrm{course}-\underline{\mathrm{fine}}}$ and ${}^{\mathrm{u/n}}E^{\mathrm{C}}_{\underline{\mathrm{coarse}}-\mathrm{fine}}$, ${}^{\mathrm{u/n}}E^{\mathrm{F}}_{\underline{\mathrm{coarse}}-\mathrm{fine}}$ respectively are obtained by normalizing ε by the maximum absolute storm surge computed over the fine grid as a function of time. For example,

$$ {}^{\mathrm{o/n}}\varepsilon = \frac{{}^{\mathrm{o}}\varepsilon}{\max(|f_{\text{fine grid}}|)}, \tag{10} $$

$$ {}^{\mathrm{u/n}}\varepsilon = \frac{{}^{\mathrm{u}}\varepsilon}{\max(|f_{\text{fine grid}}|)}. \tag{11} $$

This normalization of the error permits a relative comparison of the computations throughout the entire simulation period in addition to intra-storm comparisons. Bathymetric information at each point in time considered indicates the location of the extreme overprediction and underprediction errors and is used to identify regions where grid resolution is lacking. Table 3 summarizes the error estimates computed for each grid for the two domains considered.

4. DISCUSSION OF RESULTS

4.1. Rectangular domain

4.1.1. Hurricane H11. For meteorological forcing due to hurricane H11, extreme and normalized overprediction and underprediction errors are estimated for all grids by computing the appropriate Richardson-based error estimate. The error estimates ${}^{\mathrm{o}}E^{\mathrm{C}}_{\underline{\mathrm{coarse}}-\mathrm{fine}}$ and ${}^{\mathrm{u}}E^{\mathrm{C}}_{\underline{\mathrm{coarse}}-\mathrm{fine}}$ along with ${}^{\mathrm{o}}E^{\mathrm{F}}_{\mathrm{coarse}-\underline{\mathrm{fine}}}$ and ${}^{\mathrm{u}}E^{\mathrm{F}}_{\mathrm{coarse}-\underline{\mathrm{fine}}}$ measure the extreme overprediction and underprediction errors for the coarse grid using the fine grid solution and for the fine grid using the coarse grid solution respectively. The normalized overprediction and underprediction errors ${}^{\mathrm{o/n}}E^{\mathrm{C}}_{\underline{\mathrm{coarse}}-\mathrm{fine}}$ and ${}^{\mathrm{u/n}}E^{\mathrm{C}}_{\underline{\mathrm{coarse}}-\mathrm{fine}}$ as well as ${}^{\mathrm{o/n}}E^{\mathrm{F}}_{\mathrm{coarse}-\underline{\mathrm{fine}}}$ and ${}^{\mathrm{u/n}}E^{\mathrm{F}}_{\mathrm{coarse}-\underline{\mathrm{fine}}}$ are calculated by dividing the extreme errors by the maximum absolute storm surge computed over the fine grid over the entire simulation. In the simulations of hurricane H11 the maximum absolute surge used to compute the normalized errors ${}^{\mathrm{o/n}}E^{\mathrm{C}}_{\underline{\mathrm{coarse}}-\mathrm{fine}}$, ${}^{\mathrm{u/n}}E^{\mathrm{C}}_{\underline{\mathrm{coarse}}-\mathrm{fine}}$, ${}^{\mathrm{o/n}}E^{\mathrm{F}}_{\mathrm{coarse}-\underline{\mathrm{fine}}}$ and ${}^{\mathrm{u/n}}E^{\mathrm{F}}_{\mathrm{coarse}-\underline{\mathrm{fine}}}$ always corresponds to the peak (positive) storm surge. The four computed error estimates presented in Figures 5(a)–5(d) are for each of the regularly spaced grids G50 (Figure 5(a)), G25 (Figures 5(b) and 5(c)) and G12·5 (Figure 5(d)). In each of Figures 5(a)–5(d) the depth at the location of the extreme errors is also represented. For uniform grids G50, G25 and G12·5 the peak storm surge profiles used for normalization of the extreme errors are shown in Figure 5(e).

The errors shown in Figure 5(a) for grid G50 are based on $E^{\mathrm{C}}_{\underline{\mathrm{G50}}-\mathrm{G25}}$ which compares solutions computed over grids G50 and G25. Prior to 174 h, while the storm is predominantly located in the deep ocean, underprediction errors are more severe than overprediction errors. The extreme

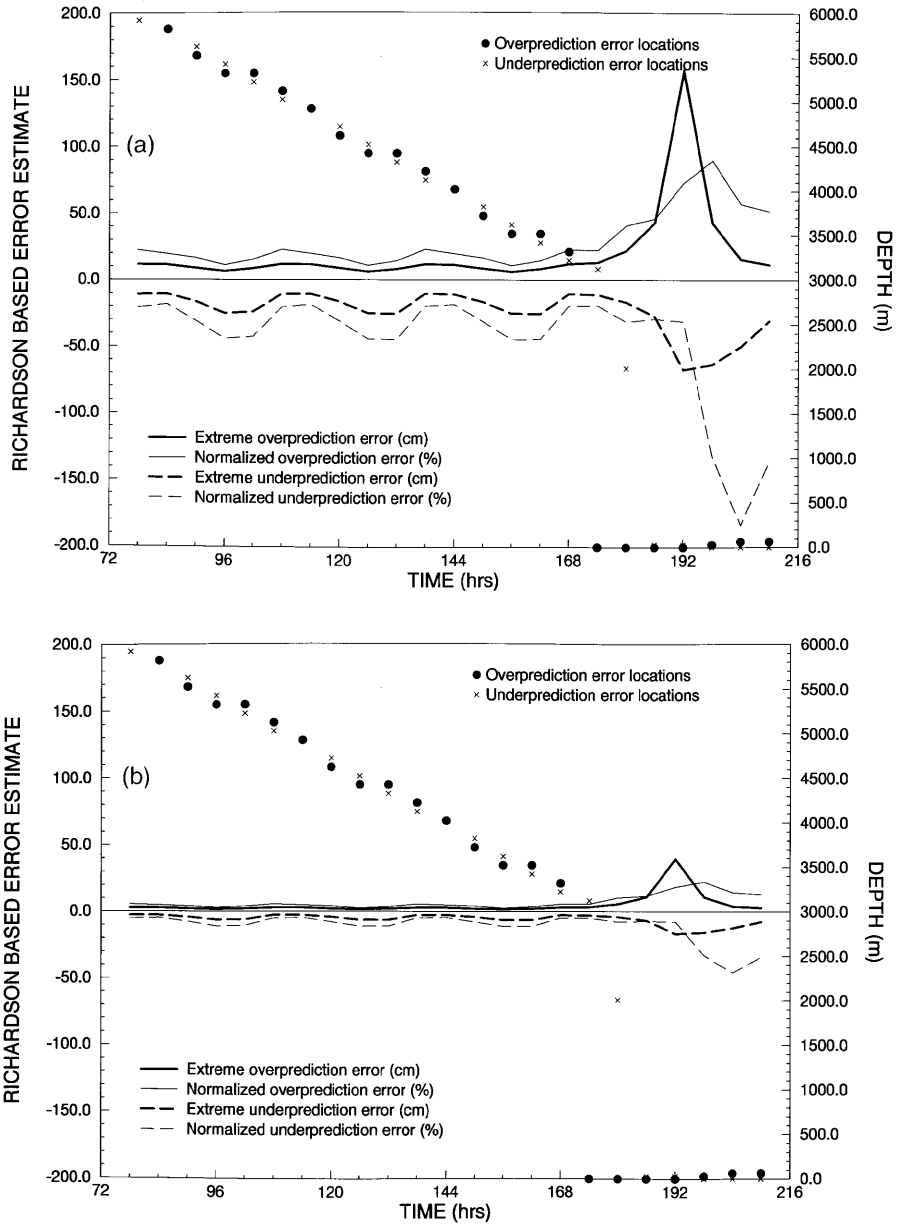

Figure 5(a–d). Extreme and normalized over- and underprediction errors in computed storm surge relative to hurricane H11 for rectangular domain grids: (a) $E^{C}_{\underline{G50}-\underline{G25}}$; (b) $E^{F}_{\underline{G50}-\underline{G25}}$; (c) $E^{C}_{\underline{G25}-\underline{G123{\cdot}5}}$; (d) $E^{F}_{\underline{G25}-\underline{G12{\cdot}5}}$

underprediction error ${}^{u}E^{C}_{\underline{G50}-G25}$ is nearly 30 cm, while the normalized underprediction error ${}^{u/n}E^{C}_{\underline{G50}-G25}$ is approximately 45%. An oscillation of the errors in the deep ocean is also observed. Similar periodic patterns can be seen in the peak storm surge profile for grid G50 (Figure 5(e)). For hurricane H11 with $R_s = 30$ km the storm is poorly resolved by a grid having a uniform spacing of 50 km. The result is a fluctuating surge which can be attributed to the inability of this coarse grid to properly interpolate the inverted barometer forcing function. This results in significant smearing or

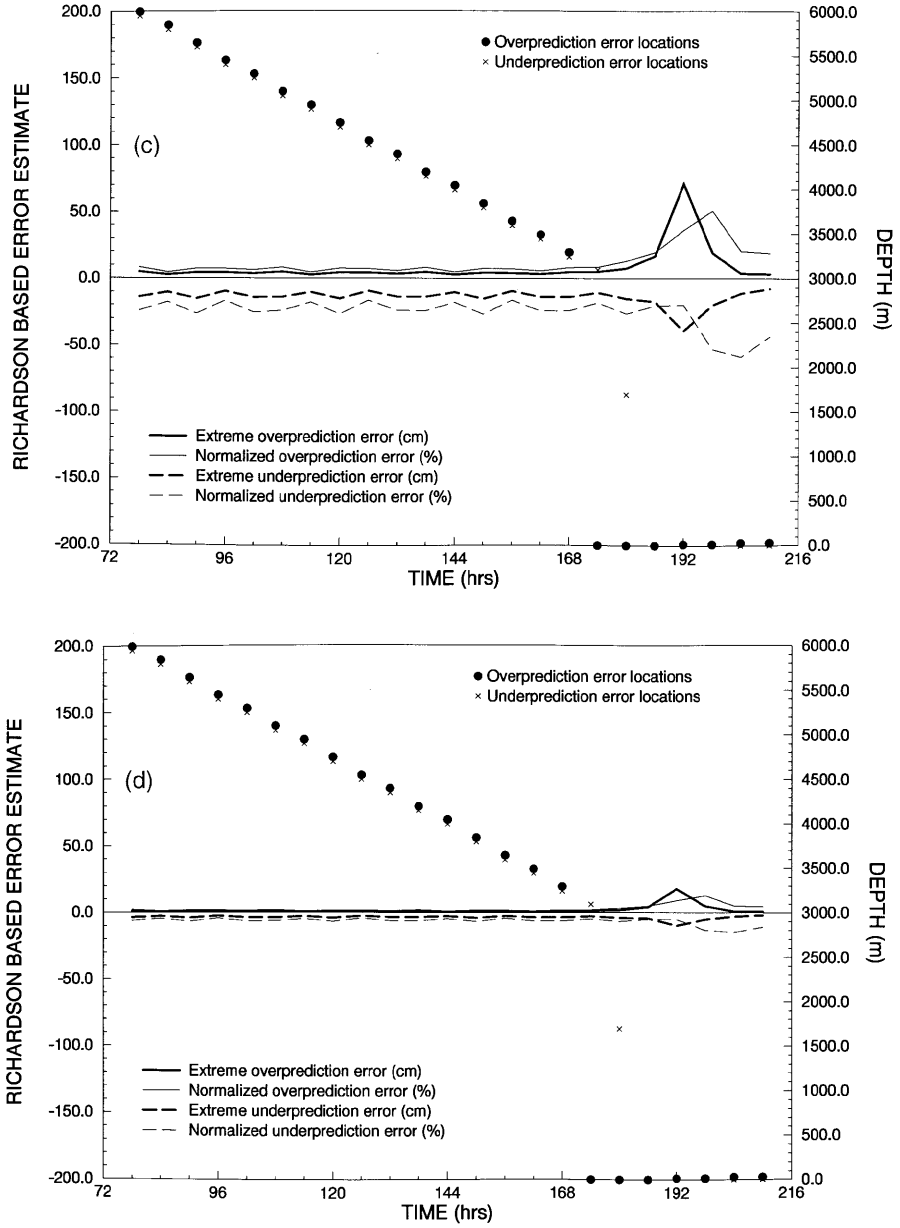

Figure 5(a–d). (*continued*)

damping of the forcing function, the degree of which is dependent on the position of the eye relative to the nodes as illustrated in Figure 6.

As the storm moves onto the continental shelf at about 180 h, extreme overprediction errors dominate as seen in Figure 5(a). Both the extreme and normalized overprediction error estimates for grid G50, ${}^{o}E^{C}_{\underline{G50}-G25}$ and ${}^{o/n}E^{C}_{\underline{G50}-G25}$, increase rapidly corresponding to the dramatic increase in storm surge generation as winds push water up onto the shelf against the coast. The largest overprediction errors, extreme and normalized, occur around the time of peak surge and are located

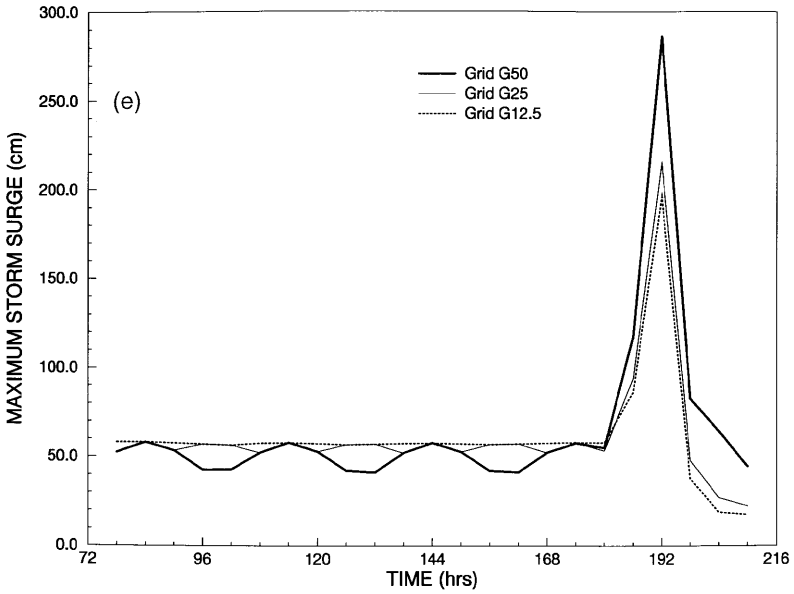

Figure 5(e). Maximum storm surge profiles for hurricane H11 computed over grids G50, G25 and G12·5

adjacent to the coastline. In fact, the most significant overprediction of the peak storm surge occurs at 192 h, the time of peak surge. The extreme overprediction error for grid G50, ${}^{o}E^{C}_{\underline{G50}-G25}$, is approximately 160 cm. The normalized overprediction error ${}^{o/n}E^{C}_{\underline{G50}-G25}$ just exceeds 70% at the time of peak surge.

After the time of peak surge the extreme overprediction and underprediction errors remain at the coastline. While the extreme errors decrease, the normalized errors continue to increase. This behaviour of the normalized error indicates that the peak surge computed over the finer grid G25 dissipates more rapidly than that computed over the coarse grid G50. This peak surge dissipation behaviour relative to grid size is also observed in Figure 5(e).

For grid G25, errors estimated by $E^{F}_{G50-\underline{G25}}$ and $E^{C}_{\underline{G25}-12\cdot5}$ are presented in Figures 5(b) and 5(c) respectively. Each of these error measures estimates the error of grid G25 using two different grid

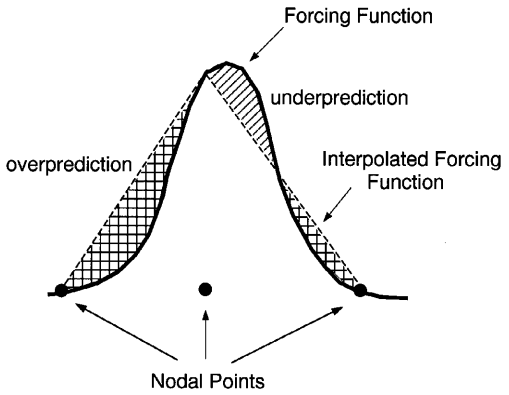

Figure 6. Schematic representation of a smeared or damped inverted barometer forcing function over a coarse grid discretization

comparisons. $E^{F}_{G50-\underline{G25}}$ represents the error for grid G25 computed using the solution from the coarse grid G50. In contrast, $E^{C}_{\underline{G25}-G12{\cdot}5}$ are the errors associated with grid G25 as estimated by comparison with the fine grid solution from grid G12·5. If the formal convergence rate (the order of the leading truncation term) matches the actual asymptotic convergence rate (i.e. there are no mechanisms which result in inter-order truncation term interaction as the grid is refined) and the grid is fine enough to be in the asymptotic range, the fine and coarse grid Richardson-based error measures $E^{F}_{G50-\underline{G25}}$ and $E^{C}_{\underline{G25}-G12{\cdot}5}$ will yield similar magnitudes.[35]

Patterns in the error estimates for G25 as given by $E^{F}_{G50-\underline{G25}}$ are the same as those computed for grid G50 using $E^{C}_{\underline{G50}-G25}$. This is expected since the error estimates for grids G50 and G25 are computed using an identical grid comparison between G50 and G25. The magnitudes of the errors for grid G25 are reduced by a factor of four owing to the resolution doubling from grid G50 to grid G25 and the relationship between $E^{F}_{G50-\underline{G25}}$ and $E^{C}_{\underline{G50}-G25}$ (i.e. $E^{F}_{G50-\underline{G25}}$ is equivalent to $\frac{1}{4}E^{C}_{\underline{G50}-G25}$).

During the period for which storm H11 is in the deep ocean (prior to 174 h), extreme underprediction errors are again more prevalent than extreme overprediction errors. For example, the largest values of ${}^{o}E^{F}_{G50-\underline{G25}}$ in the deep ocean are approximately 5 cm and the magnitude of ${}^{o/n}E^{F}_{G50-\underline{G25}}$ is less than 6%. The corresponding underprediction error ${}^{u}E^{F}_{G50-\underline{G25}}$ and ${}^{u/n}E^{F}_{G50-\underline{G25}}$ are of the order of 10 cm and 12% respectively. While the storm is on the continental shelf and storm surge generation is most intense, extreme overprediction errors are prevalent and significantly greater than underprediction errors. The extreme overprediction errors ${}^{o}E^{F}_{G50-\underline{G25}}$ reach levels of 40 cm and the normalized overprediction errors ${}^{o/n}E^{F}_{G50-\underline{G25}}$ are 20% at 192 h into the simulation. Throughout the storm period the largest extreme overprediction and underprediction errors occur at the time of peak surge. Furthermore, errors occurring while the storm is on the continental shelf are exclusively located at the shoreline and in the very-nearshore region.

As mentioned previously, estimates of the error associated with grid G25 are computed using two Richardson-based estimators, $E^{F}_{G50-\underline{G25}}$ and $E^{C}_{\underline{G25}-G12{\cdot}5}$. A comparison of Figures 5(b) and 5(c) reveals that the two error estimates for grid G25 differ by a factor of approximately two, with $E^{C}_{\underline{G25}-G12{\cdot}5}$ producing larger values. In addition to differences in error magnitudes, the error patterns seen in Figures 5(b) and 5(c) are slightly varied. In the deep ocean the oscillatory behaviour observed in Figure 5(c) for $E^{C}_{\underline{G25}-G12{\cdot}5}$ is relatively not as pronounced as that seen in the error $E^{F}_{G50-\underline{G25}}$ owing to better resolution of the pressure forcing function in deep waters over grids G25 and G12·5.

Differences in the magnitudes and deviations in the error patterns of Richardson-based error measures $E^{F}_{G50-\underline{G25}}$ and $E^{C}_{\underline{G25}-G12{\cdot}5}$ indicate that the observed convergence rates for regularly spaced grids G50, G25 and G12·5 are in fact less than the formal rate $r = 2$. This is consistent with other grid convergence studies that have been done for shallow water equations.[35] The coarse grid error estimator $E^{C}_{\underline{G25}-G12{\cdot}5}$ will be more conservative than the fine grid error estimator $E^{F}_{G50-\underline{G25}}$.

Errors estimated for grid 12·5, shown in Figure 5(d), are computed using $E^{F}_{G25-\underline{G12{\cdot}5}}$. Again the error patterns are similar to those computed for grid G25, though magnitudes of the error are now of the order of four times smaller (Figure 5(d)) than those computed for grid G25 using $E^{C}_{\underline{G25}-G12{\cdot}5}$ (Figure 5(c)). Thus the factor-of-two grid refinement when moving from grid G25 to grid G12·5 results in the fourfold decrease in error. Although extreme underprediction errors still dominate in the deeper waters, the error levels are relatively modest (i.e. ${}^{u}E^{F}_{G25-\underline{G12{\cdot}5}} \approx 5\,\text{cm}$ and ${}^{u/n}E^{F}_{G25-\underline{G12{\cdot}5}} \approx 8\%$). On the continental shelf, extreme overprediction errors are the most significant and reach their highest values at the time of peak surge, 192 h (i.e. ${}^{o}E^{F}_{G25-\underline{G12{\cdot}5}} \approx 20\,\text{cm}$ and ${}^{o/n}E^{F}_{G25-\underline{G12{\cdot}5}} \approx 10\%$). The locations of these errors persist in nearshore regions along the coastline.

Examination of the Richardson-based error estimates for the three uniformly spaced grids suggests that a graded grid structure may be most appropriate in modelling storm surge. Consistently the largest extreme and normalized errors occur on the continental shelf adjacent to the coastline. Thus a

grid having coarser resolution in the deep ocean and finer resolution in shallower waters is most appropriate.

Error estimates of the two variably graded grids VG1 and VG2 are presented in Figures 7(a) and 7(b). Both the extreme overprediction (${}^{o}E^{C}_{\underline{VG1}-CVG1}$ and ${}^{o}E^{C}_{\underline{VG2}-CVG2}$) and underprediction (${}^{u}E^{C}_{\underline{VG1}-CVG1}$ and ${}^{u}E^{C}_{\underline{VG2}-CVG2}$) errors are computed. Normalization of the extreme errors is achieved using the maximum absolute surge for the storm period which corresponds to the peak surge profiles

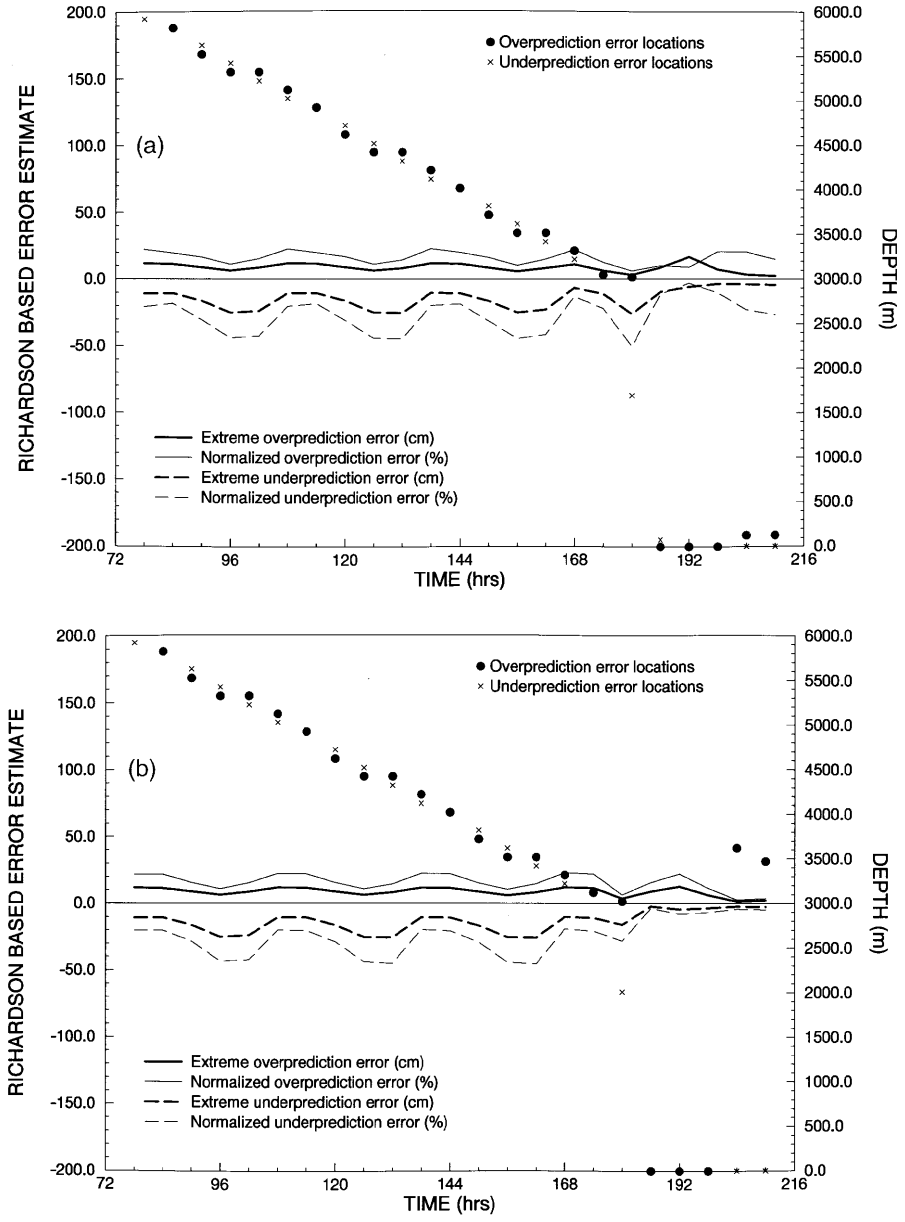

Figure 7(a,b). Extreme and normalized over- and underprediction errors in computed storm surge relative to hurricane H11 for rectangular domain variably graded grids: (a) $E^{C}_{\underline{VG1}-CVG1}$; (b) $E^{C}_{\underline{VG2}-CVG2}$

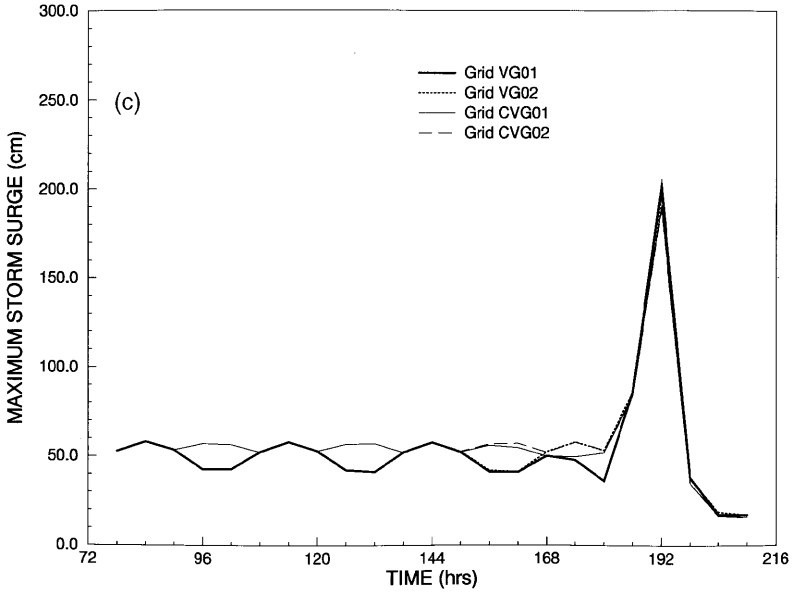

Figure 7(c). Maximum storm surge profiles for hurricance H11 computed over grids VG1, VG2, CVG1 and CVG2

associated with grids CVG1 and CVG2 shown in Figure 7(c). The normalized overprediction and underprediction errors are computed using ${}^{o/n}E^{C}_{\underline{VG1}-CVG1}$, ${}^{o/n}E^{C}_{\underline{VG2}-CVG2}$, ${}^{u/n}E^{C}_{\underline{VG1}-CVG1}$ and ${}^{u/n}E^{C}_{\underline{VG2}-CVG2}$.

For the graded grid VG1, errors in the storm surge computations over the deep ocean are the same as those computed over grid G50 since both grids have an identical grid spacing of 50 km in deep waters. As the storm moves onto the continental shelf, locations of all error measures computed for grid VG1 (Figure 7(a)) shift from deep waters to nearshore regions. During this period, overprediction errors still exceed underprediction errors. Maximum values of all errors occur at the time of peak surge and are slightly less in magnitude than those computed for grid G12·5 (i.e. ${}^{o}E^{C}_{\underline{VG1}-CVG1} \approx 18$ cm and ${}^{o/n}E^{C}_{\underline{VG1}-CVG1} \approx 8\%$). These errors occurring near the time of peak surge are located at the shoreline. Following the time of the storm's peak surge, extreme errors diminish rapidly while normalized errors persist at a modest level.

All errors computed over grid VG1 are relatively uniform in time throughout the storm duration. During the initial movement of the storm through deep waters, errors are somewhat larger than those on the shelf, but these errors are not significant in coastal regions which are of interest. On the continental shelf, maximum error estimates appear closest to the coast around the time of peak surge.

Grid VG2 extends the high level of coastal resolution provided in grid VG1 to include the entire continental shelf, the shelf break and portions of the slope. In the deep ocean the computed errors for grid VG2 are identical to those calculated for grid VG1. While the storm is in shallow waters, Richardson-based error estimates for grid VG2, shown in Figure 7(b), are somewhat lower but very similar in pattern and location to the errors computed for grid VG1. The major difference in error patterns between grids VG1 and VG2 appear to be more rapid reduction of the normalized error estimate after the time of peak surge as well as the movement of the largest errors into deep waters. Overall it appears that the higher level of resolution provided over the outer shelf in grid VG2 is not essential and that grid VG1 provides an adequate discretization which maintains relatively uniform and low errors throughout the simulation.

4.1.2. Hurricane H12. The effect of an increased storm scale on the grid resolution requirements for prediction of hurricane storm surge is investigated using forcing from hurricane H12. Recall that hurricane H12 has $R_s = 30$ km, double that of hurricane H11. For each of the five rectangular domain grids G50, G25, G12·5, VG1 and VG2 the overprediction and underprediction errors (extreme and normalized) are computed using the appropriate Richardson-based error estimate.

The effect of increasing the spatial scale of the hurricane is almost entirely limited to the deep ocean. Errors located in deep waters are reduced and oscillations previously associated with a poorly resolved inverted barometer forcing function are also diminished. From an examination of the ratio of the storm scale to the grid spacing in the deep ocean and the approximate number of nodes across the diameter of the storm for hurricanes H11 and H12, both given in Table IV, it is clear that all grids have an $R_s/\Delta x$ ratio for hurricane H12 that is double the corresponding ratio associated with hurricane H11. Furthermore, Richardson-based error estimates in deep waters computed for grids G50, G25, G12·5, VG1 and VG2 are about one-half to one-quarter the magnitude of the errors associated with hurricane H11 forcing. The large-scale storm effectively reduces the errors associated with each grid to levels associated with a grid doubling.

Computed normalized error levels in deep water are quite consistent with the maximum possible interpolation error associated with the discrete representation of the inverted barometer forcing function. The maximum interpolation error is correlated with a $\Delta x/2$ shift in the grid relative to the position of the peak forcing function. For the case $R_s/\Delta x = 0{\cdot}6$, $\Delta x \approx 2R_s$ corresponds to approximately two nodes across the scale diameter ($2R_s$) of the storm. Consequently the maximum forcing function interpolation error occurs when $\Delta x/2 \approx R_s$. Table V presents the pressure distribution, from equation (4), associated with the inverted barometer forcing as a function of distance r from the hurricane eye and the scale radius of the storm, R_s. For $r = R_s$ the pressure distribution associated with the inverted barometer forcing function is approximately 0·37 and is equivalent to the maximum interpolation error. This value reasonably approximates the computed normalized underprediction error ${}^{u/n}E^{C}_{\overline{G50}-G25}$ of 0·45 for grid G50 and storm H11 (recall from Table IV that $R_s/\Delta x = 0{\cdot}6$ for grid G50). For $R_s/\Delta x = 1{\cdot}2$, $\Delta x \approx R_s$ and the maximum forcing function interpolation error is given by $\Delta x/2 \approx R_s/2$. In Table V the pressure distribution associated with the inverted barometer forcing, and hence the maximum interpolation error for $r = R_s/2$, corresponds to approximately 0·13, which again is consistent with the computed normalized underprediction errors ${}^{u/n}E^{C}_{\overline{G25}-G12{\cdot}5}$ for storm H11 and ${}^{u/n}E^{C}_{\overline{G50}-G25}$ for storm H12 equal to 0·12.

While the storm is on the shelf, all errors and error patterns are basically similar to those estimated using hurricane H11 forcing. In relation to the grid discretization the influence of storm scale appears to be limited to deeper waters.

Table IV. Relationships between storm scale and deep ocean grid spacing for rectangular domain grids

Hurricane	Grid(s)	$R_s/\Delta x$	Approximate number of nodes across $2R_s$
H11	G50, VG1, VG2	0·6	2
	G25	1·2	3
	G12·5	2·4	5
H12	G50, VG1, VG2	1·2	3
	G25	2·4	5
	G12·5	4·8	9

Table V. Pressure distribution associated with inverted barometer forcing

r	$\frac{p_s - p_{eye}}{\bar{p} - p_{eye}} = e^{-R_s/r}$
0	0
$\frac{1}{4}R_s$	0·02
$\frac{1}{2}R_s$	0·13
R_s	0·37
$1{\cdot}2R_s$	0·43
$2{\cdot}4R_s$	0·65

4.1.3. Hurricane H13. Hurricane H13 demonstrates the effect of an increased forward speed on grid resolution requirements. The forward speed of hurricane H13 is 1·67 times that of hurricane H11, while the spatial scale is identical to that of storm H11. The extreme and normalized error estimates of the overprediction and underprediction of the storm surge are computed for each grid G50, G25, G12·5, VG1 and VG2. All prediction errors are very similar in pattern and magnitude to those reported for hurricane H11 and indicate underresolution of the inverted barometer forcing in deep water and the largest errors occur nearest to the coastline at the time of peak surge. Errors produced by the faster storm H13 exhibit similar patterns over a shortened time scale as errors computed for hurricane H11 and H12 forcings.

4.1.4. Hurricane H31. The influence of the hurricane path on storm surge generation and subsequent grid resolution requirements is examined by applying the forcing from hurricane H31. Hurricane H31 approaches the shoreline at an angle and then moves parallel to the shelf break and coast with the hurricane eye centred 60 km offshore. The spatial scale of hurricane H31, given by $R_s = 30$ km, results in maximum winds remaining on the continental shelf approximately 30 km offshore. The four Richardson-based error measures used previously are computed for all grids in an identical manner as was done for hurricanes H11, H12 and H13.

As the storm moves through the deep ocean and approaches the continental shelf, errors are located in deep water and have similar patterns and magnitudes as those shown for the error estimates computed relative to forcing for hurricane H11. In fact, grids G50, VG1 and VG2 have identical errors in the storm surge computation over deep water since they have the same spacing of 50 km in deep waters. Underprediction of the inverted barometer effect in the surge elevations results from significant underresolution of the inverted barometer forcing function and is the predominant error feature in deep water.

As the storm moves shoreward and parallels the coast, relatively uniform error estimates over the storm period occur at the coastline for grids G50, G25 and G12·5. Overprediction of the peak curve is again the primary feature of shelf errors. Error reduction patterns with increasing grid refinement are very similar to those seen using the three previous hurricanes, except that both absolute and normalized peak errors are now sustained while the storm moves parallel to the shore.

Extreme and normalized errors are nearly the same for each unstructured grid VG1 and VG2 while the storm is on the continental shelf, a consequence of the smaller surges generated by a storm tracking parallel to the coast. Underprediction and overprediction error of the storm surge are equal in magnitude and remain uniform over each of grids VG1 and VG2 as the storm parallels the coast. Richardson-based error estimates for grid VG1 are quite low and predominantly located at the

coastline, while errors computed over grid VG2 are reduced even further and their locations are shifted into deep waters.

The surge elevations generated by a storm moving parallel to the coastline may be less than those created by a landfalling hurricane, but errors in the computation of storm surge indicate that grid resolution near the shore is still of primary importance.

4.2. Rectangular domain with sinusoidal coastline

The series of grids using the rectangular domain with a sinusoidal coastline is designed to establish the influence of shoreline variability on storm surge generation and storm surge prediction errors. Normalized and extreme overprediction and underprediction error measures based on Richardson extrapolation are computed for the three uniform grids G50_C5, G25_C9 and G12·5_C17 and are shown in Figures 8(a)–8(d) for hurricane H11 forcing. The peak storm surge values for hurricane H11 used to obtain normalized error estimates are shown in Figure 8(e).

For all three grids the error estimates in deep water clearly exhibit a dominant underprediction of the inverted barometer effect in the storm surge associated with the smearing or damping of the inverted barometer forcing function. Magnitudes of all errors as well as error patterns in the deep ocean are quite similar to those computed using the rectangular domain grids, indicating that variability of the coastline does not significantly effect storm surge generation in deep waters.

As the storm moves across the continental shelf, the largest errors over all three grids reflect an overprediction of the storm surge. Generally, error estimates in Figures 8(a)–8(d) follow the trends established for the rectangular domain uniform grids. For grid G50_C5, overprediction errors are estimated using ${}^{\mathrm{o}}E^{\mathrm{C}}_{\underline{\mathrm{G50\_C5}}-\mathrm{G25\_C9}}$ and ${}^{\mathrm{o/n}}E^{\mathrm{C}}_{\underline{\mathrm{G50\_C5}}-\mathrm{G25\_C9}}$ and underprediction errors are obtained from the ${}^{\mathrm{u}}E^{\mathrm{C}}_{\underline{\mathrm{G50\_C5}}-\mathrm{G25\_C9}}$ and ${}^{\mathrm{u/n}}E^{\mathrm{C}}_{\underline{\mathrm{G50\_C5}}-\mathrm{G25\_C9}}$ indices shown in Figure 8(a). Note the expanded scale for the error magnitudes in Figure 8(a). Clearly, for errors incurred while the storm is on the continental shelf, overprediction is the dominant feature. Maximum overprediction errors occur at the time of peak surge and have values of 350 cm for the extreme error ${}^{\mathrm{o}}E^{\mathrm{C}}_{\underline{\mathrm{G50\_C5}}-\mathrm{G25\_C9}}$ and 85% for the normalized error ${}^{\mathrm{o/n}}E^{\mathrm{C}}_{\underline{\mathrm{G50\_C5}}-\mathrm{G25\_C9}}$. Extreme errors computed using grid G50_C5 are significantly larger than those computed for grid G50 which has a straight-line coast. Even though the sinusoidal variations in the coastline are more effective than the straight-line coast in building up water along the shore (as seen in the peak storm surge profile, Figure 8(e)), maximum normalized errors associated with the sinusoidal coastline grid G50_C5 are approximately the same as for the straight-line coast domain.

Error estimates for grid G25_C9, seen in Figures 8(b) and 8(c), are made using a fine index $E^{\mathrm{F}}_{\mathrm{G50\_C5}-\underline{\mathrm{G25\_C9}}}$ and a coarse index $E^{\mathrm{C}}_{\underline{\mathrm{G25\_C9}}-\mathrm{G12{\cdot}5\_C17}}$ respectively. The fine grid error estimates for grid G25_C9 (Figure 8(b)) have patterns which are the same as those computed for grid G50_C5 (Figure 8(a)). The error magnitudes for grid G25_C9, however, are reduced by a factor of four (i.e. ${}^{\mathrm{o}}E^{\mathrm{F}}_{\mathrm{G50\_C5}-\underline{\mathrm{G25\_C9}}} \approx 90$ cm and ${}^{\mathrm{o/n}}E^{\mathrm{F}}_{\mathrm{G50\_C5}-\underline{\mathrm{G25\_C9}}} \approx 20\%$) when comparing error estimates for grid G50_C5. Comparison of the errors in Figures 8(b) and 8(c) indicates that both the fine and coarse error measures for grid G25_C9 yield values that differ by a factor of approximately two in deep water as was the case for the straight-line coast domain. However, the fine and coarse error estimates for grid G25_C9 on the continental shelf are quite similar when compared with the corresponding fine and coarse grid errors computed for grid G25, $E^{\mathrm{F}}_{\mathrm{G50}-\underline{\mathrm{G25}}}$ and $E^{\mathrm{C}}_{\underline{\mathrm{G25}}-\mathrm{G12{\cdot}5}}$. The coarse index $E^{\mathrm{C}}_{\underline{\mathrm{G25\_C9}}-\mathrm{G12{\cdot}5\_C17}}$ remains the larger of the two error estimates but not by a factor of two as reported for grid G25. Thus it appears that for the domains with a sinusoidal land boundary the formal convergence rate equals the actual observed convergence rate for the continental shelf response. It is interesting to note that this was not the case for the straight coastline domains examined. The behaviour of the coarse and fine grid error estimates for the sinusoidal land boundary domain

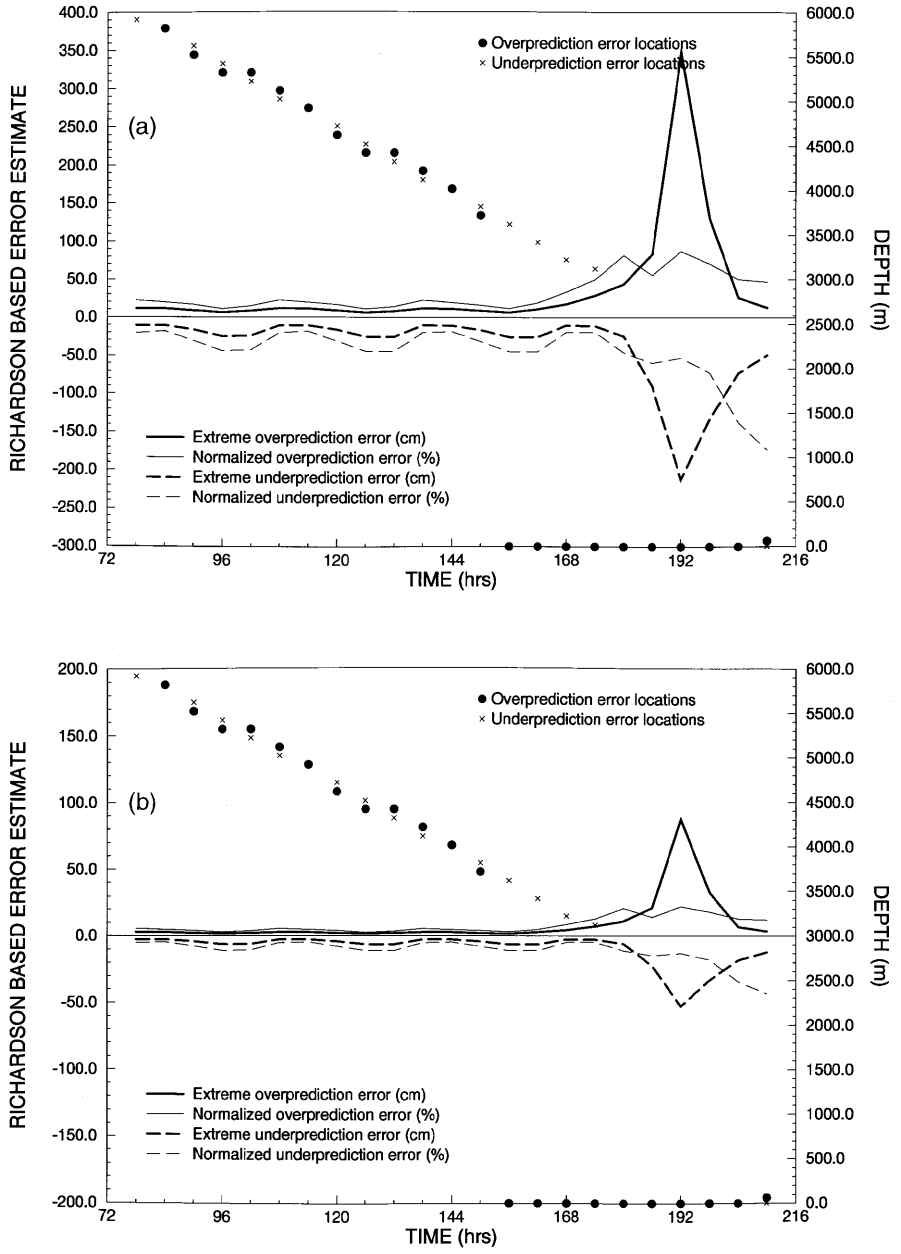

Figure 8(a–d). Extreme and normalized over- and underprediction errors in computed storm surge relative to hurricane H11 for rectangular domain grids having a sinusoidally varying coastline: (a) $E^{C}_{\underline{G50\_C5}-G25\_C9}$; (b) $E^{F}_{G50\_C5-\underline{G25\_C9}}$; (c) $E^{C}_{\underline{G25\_C9}-G12{\cdot}5\_C17}$; (d) $E^{F}_{G25\_C9-\underline{G12{\cdot}5\_C17}}$

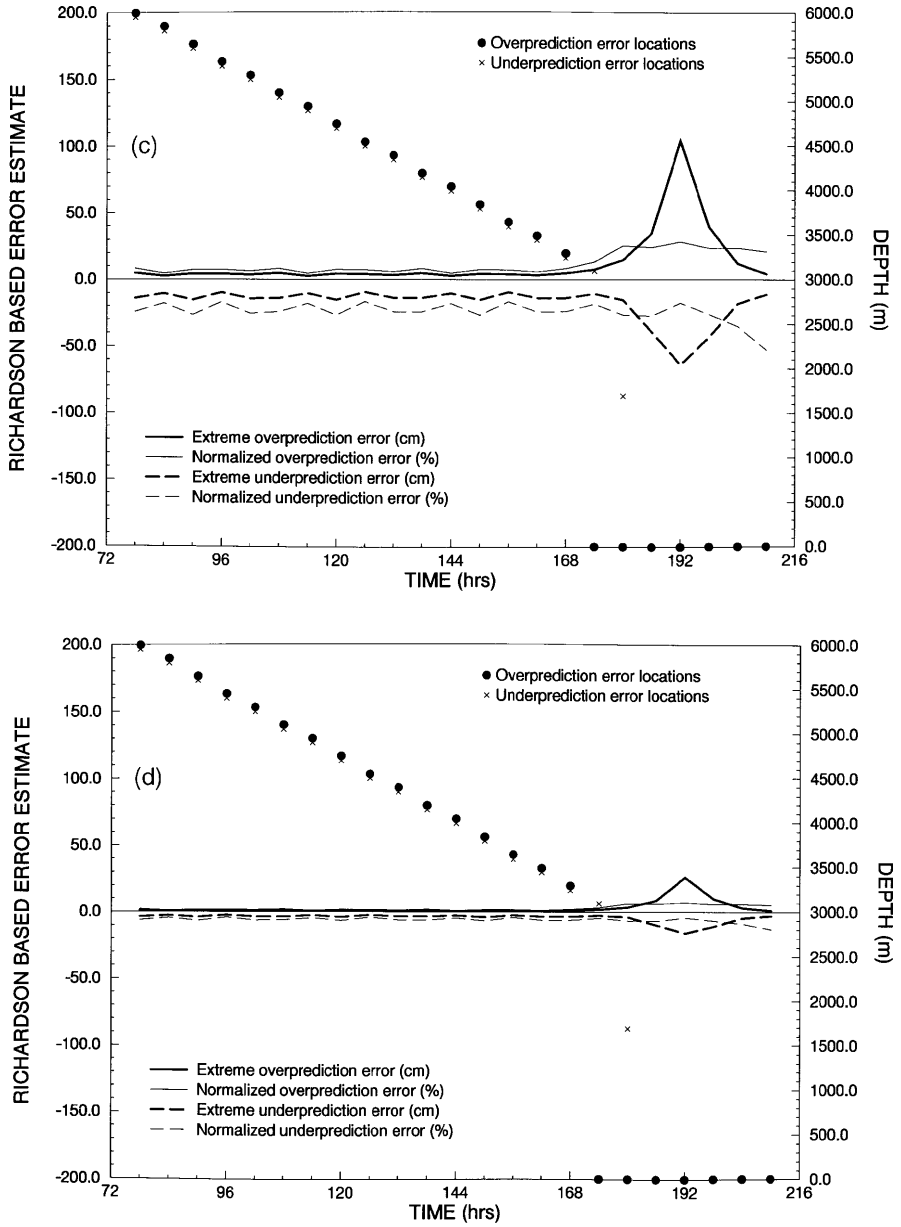

Figure 8(a–d). (*continued*)

G25_C9 may be due in part to the fact that the error estimates for grids G50_C5, G25_C9 and G12·5_C17 are the result of truncation errors which are associated with grid spacing as well as truncation errors associated with the representation of the coastal boundary. Separate simulations using grids G12·5_C5, G12·5_C9 and G12·5_C17 which have three levels of shoreline boundary refinement indicate that a significant, though not dominant, portion of the shelf errors is related to resolution of the coastal boundary.

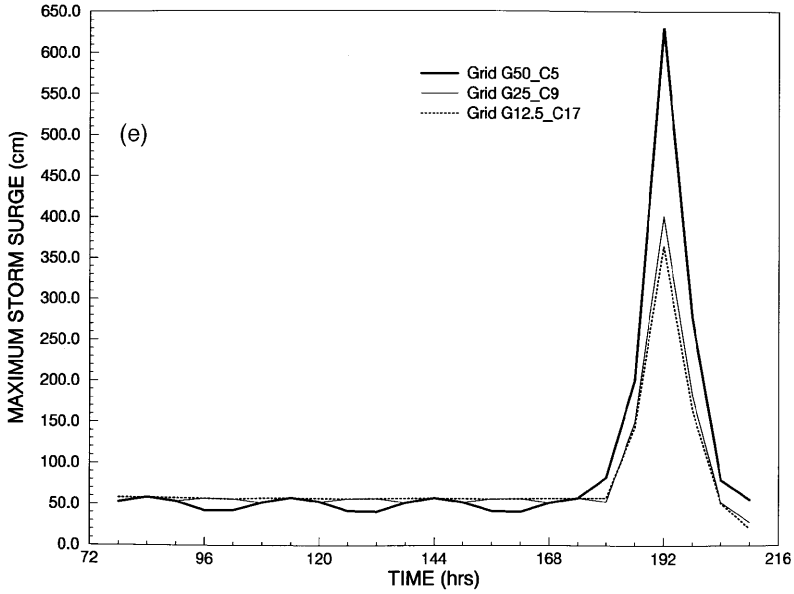

Figure 8(e). Maximum storm surge profiles for hurricane H11 computed over grids G50_C5, G25_C9 and G12·5_C17

For grid G12·5_C17, extreme and normalized overprediction and underprediction errors are shown in Figure 8(d) and exhibit the trends seen in the error estimates for grid G25_C9 (e.g. overprediction is the major source of error in the coastal ocean). Magnitudes of all errors are reduced fourfold over those computed for grid G25_C9 (i.e. ${}^{o}E^{F}_{G25\_C9-\underline{G12{\cdot}5\_C17}} \approx 28\,\text{cm}$ and ${}^{o/n}E^{F}_{G25\_C9-\underline{G12{\cdot}5\_C17}} \approx 8\%$).

Error estimates for the variably graded grids VG1_C17 and VG2_C127 are displayed in Figures 9(a) and 9(b). Both extreme and normalized overprediction and underprediction errors are computed. The maximum storm surge values used to obtain the normalized errors are shown in the storm surge hydrographs for grids CVG1 and CVG2 (Figures 9(c)). In Figures 9(a) and 9(b), errors located in deep water have a similar pattern and behaviour as those errors computed for the corresponding rectangular domain grids VG1 and VG2 as well as the coarse grids G50 and G50_C5. Again, underprediction errors are largest while the storm is in the deep ocean, with values of approximately 30 cm for ${}^{u}E^{C}$ and 45% for ${}^{u/n}E^{C}$.

For the period when the storm is on the continental shelf, overprediction is the dominant error for both grids VG1_C17 and VG2_C17. Extreme overprediction errors are significantly greater than those estimated for the variably graded grids having a straight-line coast. This is largely due to the increased peak surge generated by the sinusoidally varying coastline. Note, however, that normalized errors (e.g. ${}^{u/n}E^{C}_{\underline{VG1\_C17}-CVG1\_C17} \approx 12\%$ and ${}^{u/n}E^{C}_{\underline{VG2\_C17}-CVG2\_C17} \approx 10\%$) are similar in magnitude to the normalized errors computed for the straight-line coast variably graded grids. Error estimates for grid VG2_C17, seen in Figure 9(b), are not dramatically different from those shown for grid VG1_C17 despite the increased resolution of the outer shelf, shelf break and portions of the slope provided by grid VG2_C17. Note that for variably graded grids VG1_C17 and VG2_C17 the coastline is always resolved at the highest level with 17 points per wavelength, which significantly reduces errors associated with the representation of the coastline. In general it appears that nearshore resolution is the most critical factor in determining storm surge accuracy on the continental shelf.

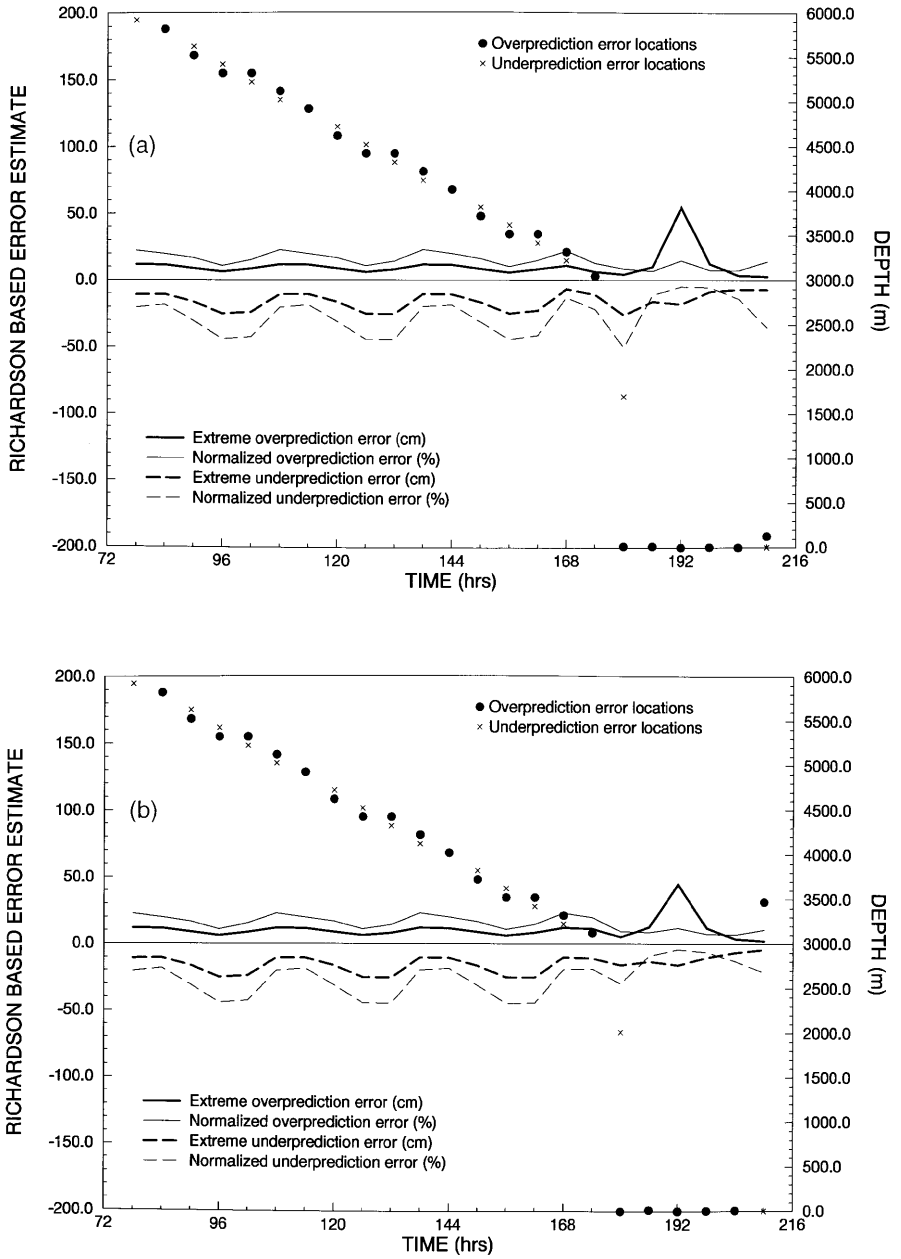

Figure 9(a,b). Extreme and normalized over- and underprediction errors in computed storm surge relative to hurricane H11 for rectangular domain variably graded grids having a sinusoidally varying coastline: (a) $E^{C}_{\underline{VG1\_C17}-CVG1\_C17}$; (b) $E^{C}_{\underline{VG2\_C17}-CVG2\_C17}$

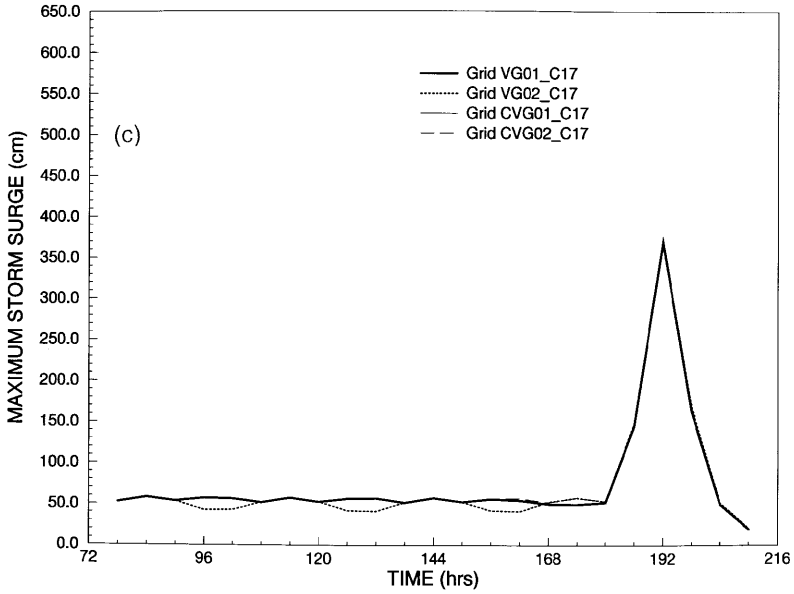

Figure 9(c). Maximum storm surge profiles for hurricane H11 computed over grids VG1_C17, VG2_C17, CVG1_C17 and CVG2_C17

5. APPLICATION OF GRIDDING STRATEGY

The general concepts for the construction of graded grids developed for the idealized rectangular domain are now applied in the simulation of Hurricane Camille, a historical storm which made landfall near Biloxi, Mississippi along the Gulf Coast of the United States. This application demonstrates the utility of the gridding strategy and reinforces that underresolution near the coastline leads to overprediction of the primary storm surge, whereas underresolution in deep water causes smearing and damping of the inverted barometer forcing function and thus underprediction of the storm surge.

5.1. Domain and grid construction

The domain selected encompasses the Gulf of Mexico, continguous basins and extends out of resonant basins into the deep regions of the western North Atlantic Ocean. This very large domain allows proper generation and propagation of storm surge into coastal regions and is similar to that used in the domain size sensitivity study of Blain *et al.*[23] A deep Atlantic Ocean boundary lies along the 60°W meridian and all other boundaries are defined by the eastern coastlines of North, Central and South America. Bathymetry is obtained from the topographic database ETOPO5 from the National Center for Atmospheric Research and supplemented in Gulf coastal regions by the NOAA Digital U.S. Coastal Hydrography sounding database. Highly detailed shoreline co-ordinates along the coast of the Gulf of Mexico are obtained from the CIA database and NOAA bathymetric charts.

A discrete representation of the domain, grid SG01, is constructed using 23,566 nodes and 43,238 elements. The variably graded structure of the SG01 discretization shown in Figure 10(a) has nodal spacings that range from a maximum of 98 km in the deep Atlantic Ocean to a maximum of 50 km in the Gulf of Mexico to a minimum of 0·5 km in selected coastal areas. Details of the resolution provided by grid SG01 in the landfall region of Hurricane Camille are shown in Figure 10(b).

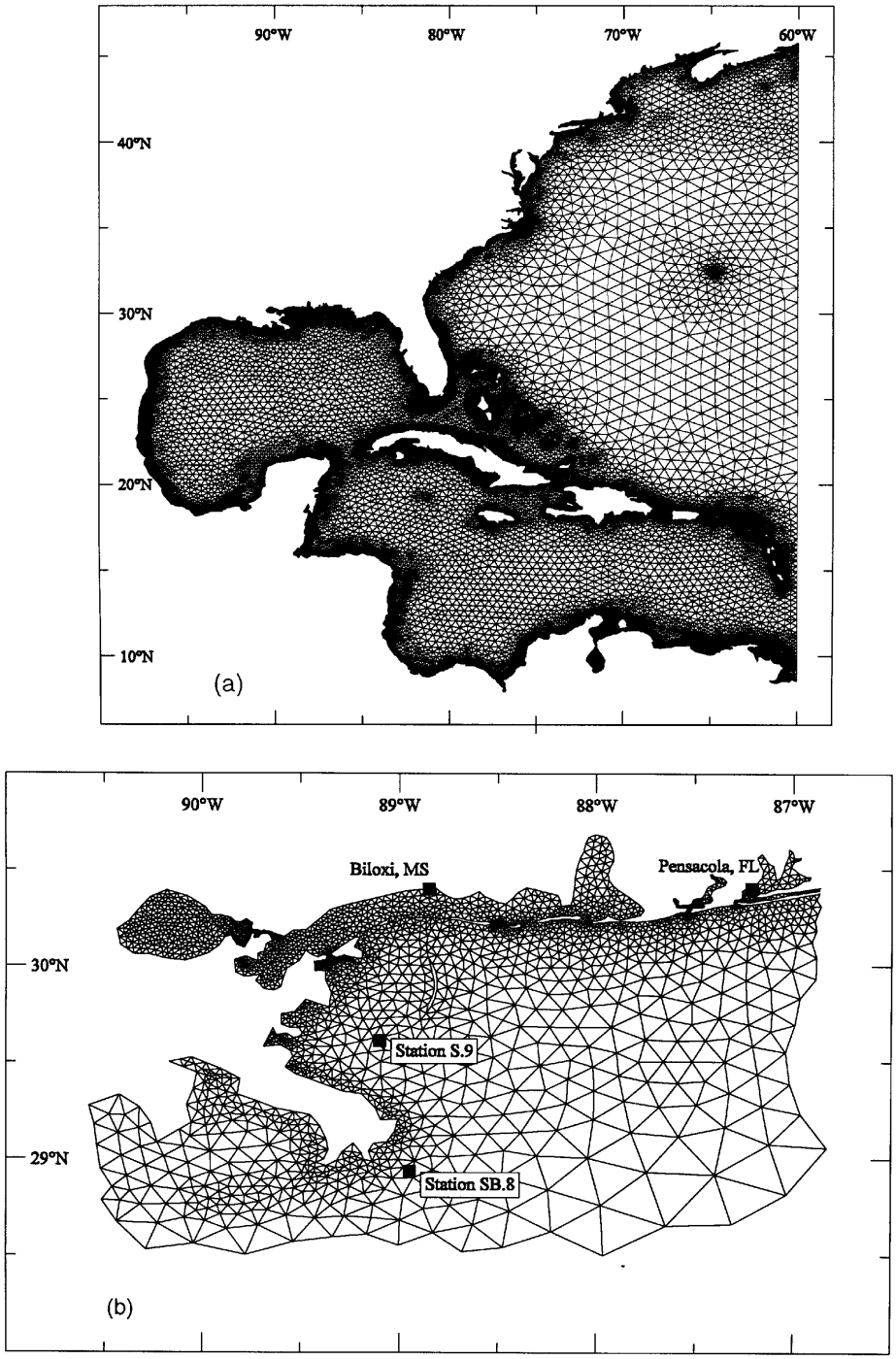

Figure 10. (a) Discretization for grid SG01. (b) Coastline detail and nearshore discretization for grid SG01 in northeast Gulf of Mexico near Biloxi, Mississippi as well as locations of four hydrograph stations

In addition to grid SG01, a highly refined comparison grid, CG01, is constructed using 90,435 nodes and 179,952 elements. Grid CG01 has a resolution which is exactly a twofold increase over that provided by grid SG01, resulting in a fourfold increase in nodal density. Grid CG01 is used to assess the convergence of grid SG01 by computing the Richardson-based error estimates defined in the previous sections.

5.2. Storm surge simulations

Hurricane Camille serves as the meteorological forcing for the hydrodynamic model. The track of Hurricane Camille through the western Caribbean Sea and Gulf of Mexico is shown at 6 h increments in Figure 11. For Hurricane Camille, model computations begin at 12:00 GMT 14 August 1969 and run for 8 days (including the 1 day ramp-up period). For the period simulated, the forward speed of Hurricane Camille ranges from 3.1 to 20·6 m s^{-1} and a radius to maximum wind is maintained at approximately 43 km. Landfall of Hurricane Camille occurs at 0:00 GMT 18 August 1969. All other parameters pertaining to Hurricane Camille were obtained from the HURDAT tape[36] which documents the movement and characteristics of historical hurricanes.

Along the open ocean boundary an inverted barometer pressure forcing is applied. The advective terms were not considered in this simulation owing to stability constraints, leaving bottom friction as the remaining non-linearity. The bottom friction coefficient is constant and equal to 0·003 and the GWCE parameter τ_0 is set equal to 0·001.

Simulations are spun up from homogeneous initial conditions using a 1 day ramp in time. An identical ramp function of 1 day length is applied to the wind and pressure forcing as well as the inverted barometer boundary condition. During the first 6 h of each simulation the initial hurricane wind and pressure fields are held stationary. Thereafter, storm surge computations use time-varying

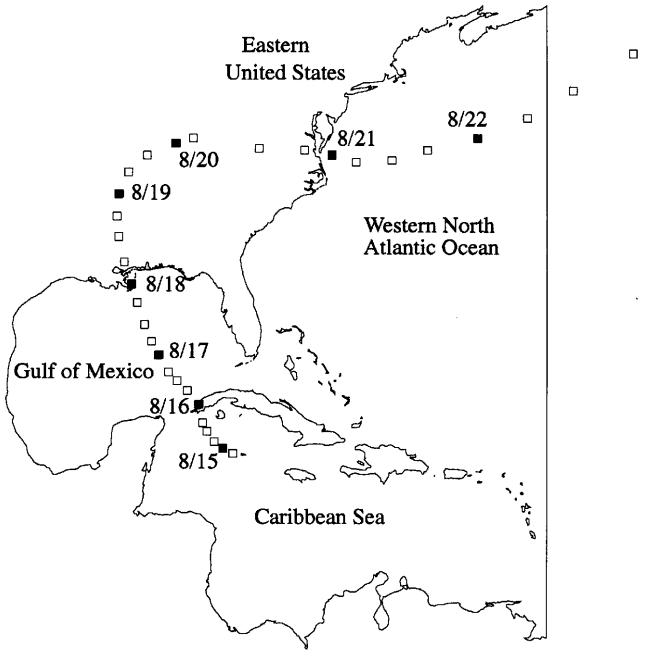

Figure 11. Track of Hurricane Camille through western Caribbean Sea and Gulf of Mexico from 18:00 GMT 14 August 1969 to 18:00 GMT 22 August 1969 shown at 6 h intervals

wind and pressure fields. The time step for simulations over grid SG01 is 45 s. This time step length is halved to 22.5 s for simulations using grid CG01. These time steps ensure that truncation errors for the grids considered are predominantly spatial discretization errors.

5.3. *Discussion of grid performance*

The magnitudes of the extreme and normalized overprediction and underprediction errors and the depths at which they occur are computed over grid SG01 in terms of a Richardson-based error estimate. The four error measures previously defined, ${}^{\mathrm{o}}E^{\mathrm{C}}_{\underline{\mathrm{SG01}}-\mathrm{CG01}}$, ${}^{\mathrm{u}}E^{\mathrm{C}}_{\underline{\mathrm{SG01}}-\mathrm{CG01}}$, ${}^{\mathrm{o/n}}E^{\mathrm{C}}_{\underline{\mathrm{SG01}}-\mathrm{CG01}}$ and ${}^{\mathrm{u/n}}E^{\mathrm{C}}_{\underline{\mathrm{SG01}}-\mathrm{CG01}}$, are calculated throughout the simulation of Hurricane Camille and are shown in Figure 12.

Both the grid convergence study and theoretical forcing function error estimates indicate that in order to capture the inverted barometer effect of the hurricane over deep waters to within approximately 12%, a level of grid resolution at least equal to the spatial scale of the hurricane is required. The tracking of Hurricane Camille begins near Cuba and follows a path over the deep portions of the Gulf of Mexico where the maximum grid spacing is approximately 45 km. Since Hurricane Camille maintains a moderate spatial scale of approximately 43 km, an $R_{\mathrm{s}}/\Delta x$ ratio of nearly one occurs over the deep waters of the Gulf of Mexico. Figure 12 shows that normalized underprediction errors for grid SG01 are limited to 20% and in fact do not occur in the deep ocean but are located adjacent to the coast. Thus the level of resolution over deep Gulf of Mexico waters is adequate to capture the inverted barometer effect of Hurricane Camille.

Figure 12 indicates that between 0:00 GMT 16 August 1969 and the time prior to peak surge development, which begins at 12:00 GMT 17 August 1969, both overprediction and underprediction errors are significant and occur adjacent to the shore. Normalized error estimates are in the 20% range and remain fairly uniform during the approach and movement of Hurricane Camille through the Gulf

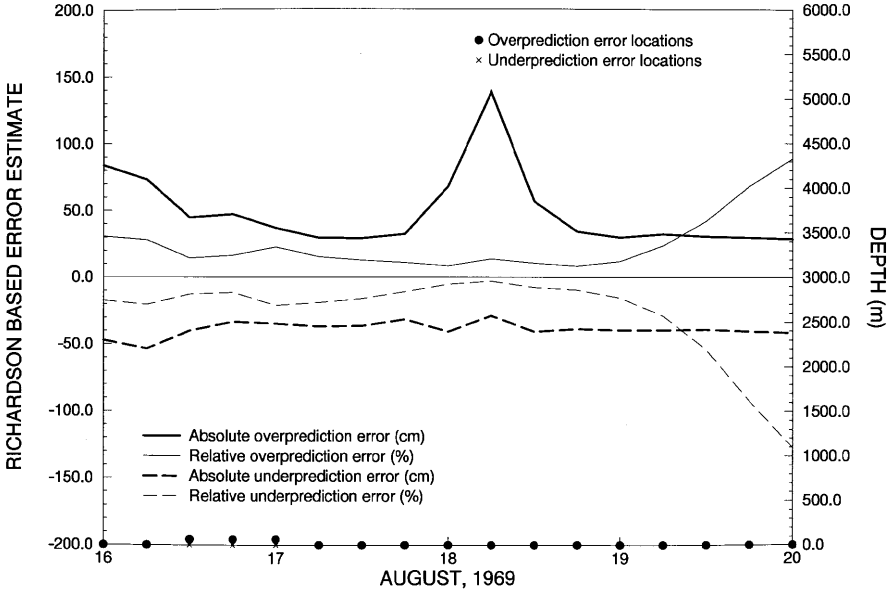

Figure 12. Extreme and normalized over- and underprediction errors in computed storm surge relative to Hurricane Camille for grid SG01, $E^{\mathrm{C}}_{\underline{\mathrm{SG01}}-\mathrm{CG01}}$

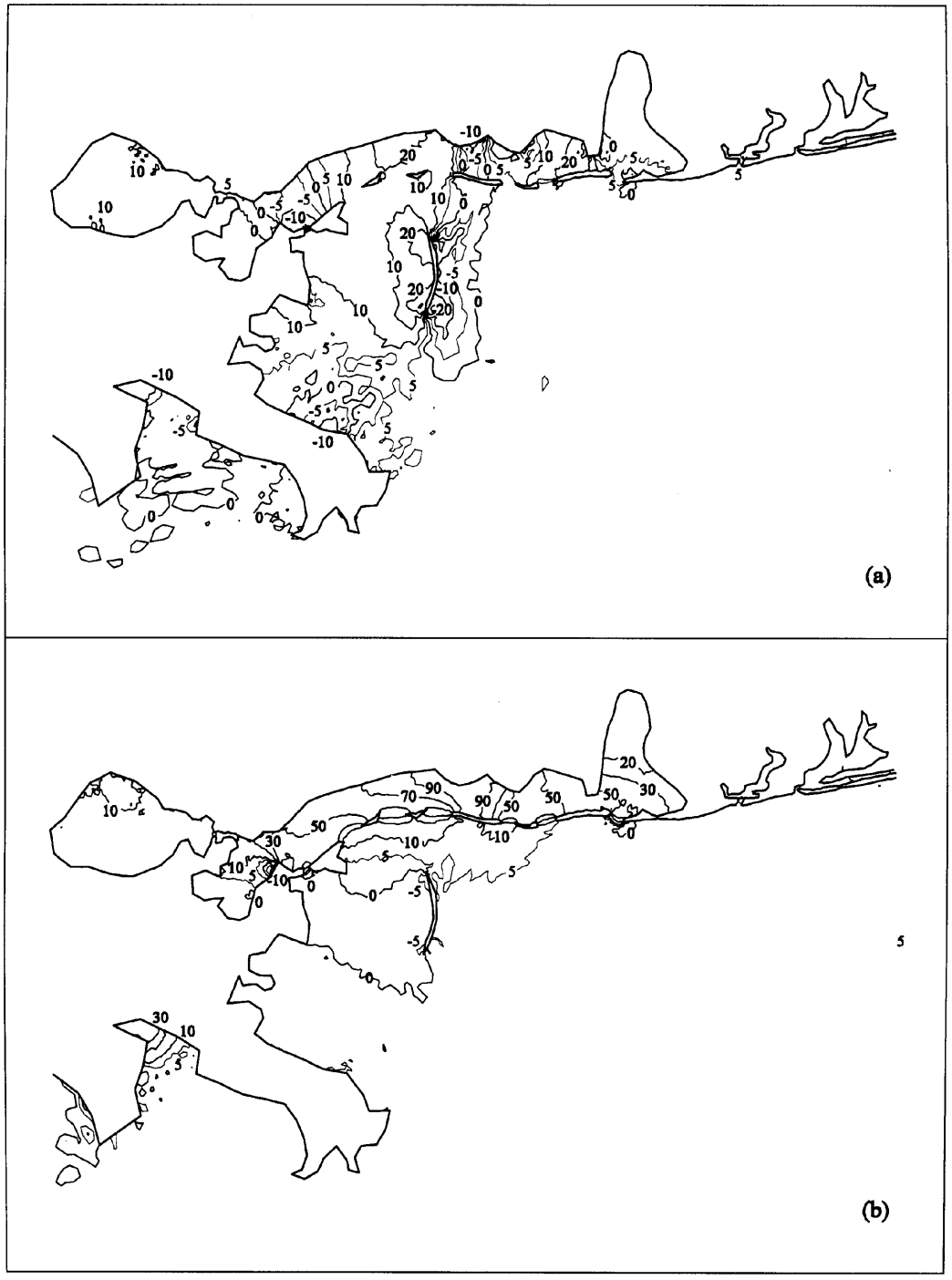

Figure 13. Contours of estimated over- and underprediction errors in storm surge computed over grid SG01 at (a) 18:00 GMT 17 August 1969 and (b) 0:00 GMT 18 August 1969 for Hurricane Camille

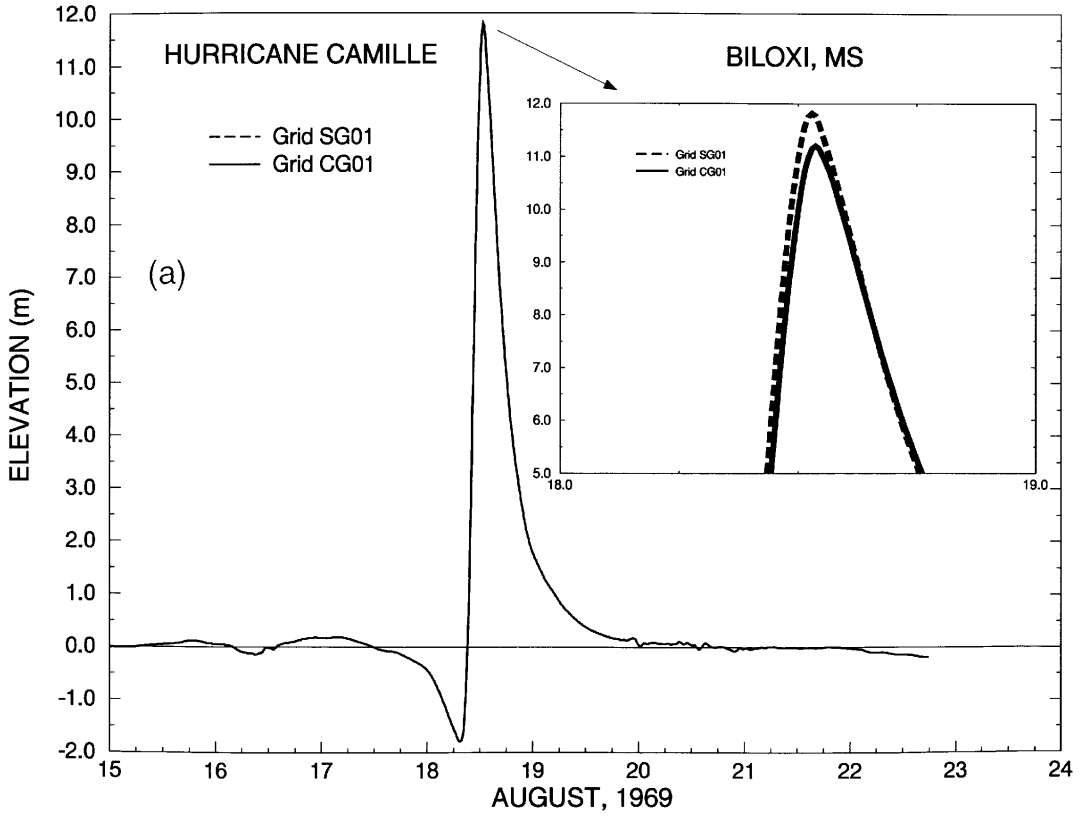

Figure 14. Storm surge hydrographs comparing computations over grids SG01 and CG01 at (a) Biloxi, Mississippi, (b) Pensacola, Florida, (c) station S.9 and (d) station SB.8

of Mexico. Patterns of the error during this period are typical of a storm following a parallel track. In fact, Figure 11 shows that Camille is moving parallel to regions along the Florida shelf at these times.

Peak storm surge development begins at 12:00 GMT 17 August 1969 when Camille starts to make landfall in a shore-perpendicular fashion. At the time of peak surge, extreme overprediction errors dominate and have values of nearly 140 cm. Normalized errors, however, are at levels of only 15% as Hurricane Camille approaches the coast and makes landfall. A rise in the normalized errors following the peak surge is due to a combination of residual errors at the coastline following landfall of the hurricane and the presence of minimal surge elevations as the hurricane moves inland. The uniform profile of the normalized prediction errors associated with Hurricane Camille's movement through the Gulf of Mexico indicates that the spatial resolution provided by grid SG01 in the nearshore regions is sufficient to maintain a constant error percentage throughout the duration of the storm. High magnitudes of the extreme overprediction error at the time of peak surge warrant examination of the spatial distribution of storm surge prediction errors throughout the domain.

Contour plots of the spatial distribution of computed elevation differences $\varepsilon = f_{\mathrm{SG01}} - f_{\mathrm{CG01}}$, shown in Figures 13(a) and 13(b), depict the estimated overprediction and underprediction errors in the storm surge computed over grid SG01 at 18:00 GMT 17 August 1969 and 0:00 GMT 18 August 1969. On 17 August 1969 at 18:00 GMT (Figure 13(a)), errors build around an island directly in the path of Hurricane Camille where resolution is relatively coarse. Six hours later (Figure 13(b)), overprediction of the storm surge reaches the 1 m level in a localized area between the coastline and

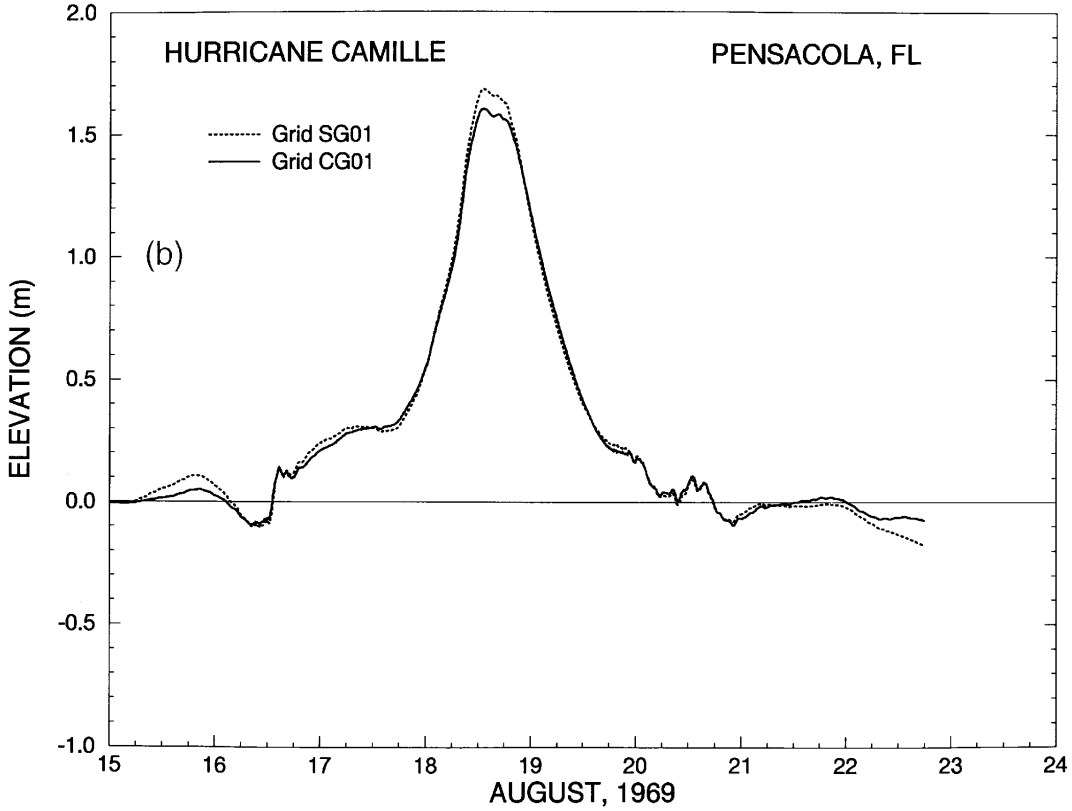

Figure 14. (*contined*)

the offshore barrier islands near Biloxi, Mississippi. Generally the spatial distribution of the error indicates that additional resolution around offshore islands and in coastal areas near the landfall point of Hurricane Camille is needed in order to reduce extreme error levels to below 1 m.

Locations in the Gulf of Mexico (shown in Figure 10(b)) of four representative storm surge hydrographs, at Biloxi, Pensacola, station S.9 on the continental shelf and station SB.8 along the shelf break, are given in Figures 14(a)–14(d). Each hydrograph compares the storm surge elevations computed over grid SG01 with those computed over the comparison grid CG01. The peak storm surge is always overpredicted, with a maximum difference between solutions computed over grids SG01 and CG01 approximately equal to 70 cm at Biloxi, Mississippi (Figure 14(a)). In comparing the elevations at Biloxi and Pensacola, Figures 14(a) and 14(b), overprediction of the storm surge increases with proximity to the landfall location of Hurricane Camille. At station S.9 on the continental shelf and station SB.8 at the shelf break, Figures 14(c) and 14(d), the predictions of peak surge over grid SG01 more closely match storm surge elevations computed over grid CG01. Furthermore, representation of the surge forerunner over grid SG01 differs by less than 5 cm from storm surge elevations computed over grid CG01.

The most significant errors in the simulation of Hurricane Camille over grid SG01 are in regions where grid refinement near the coast is coarse and the detail of the shoreline is more complex. Overall, normalized errors in the storm surge elevations computed over grid SG01 are uniform and modest in the nearshore region throughout the simulation. Further refinement in coastal areas near

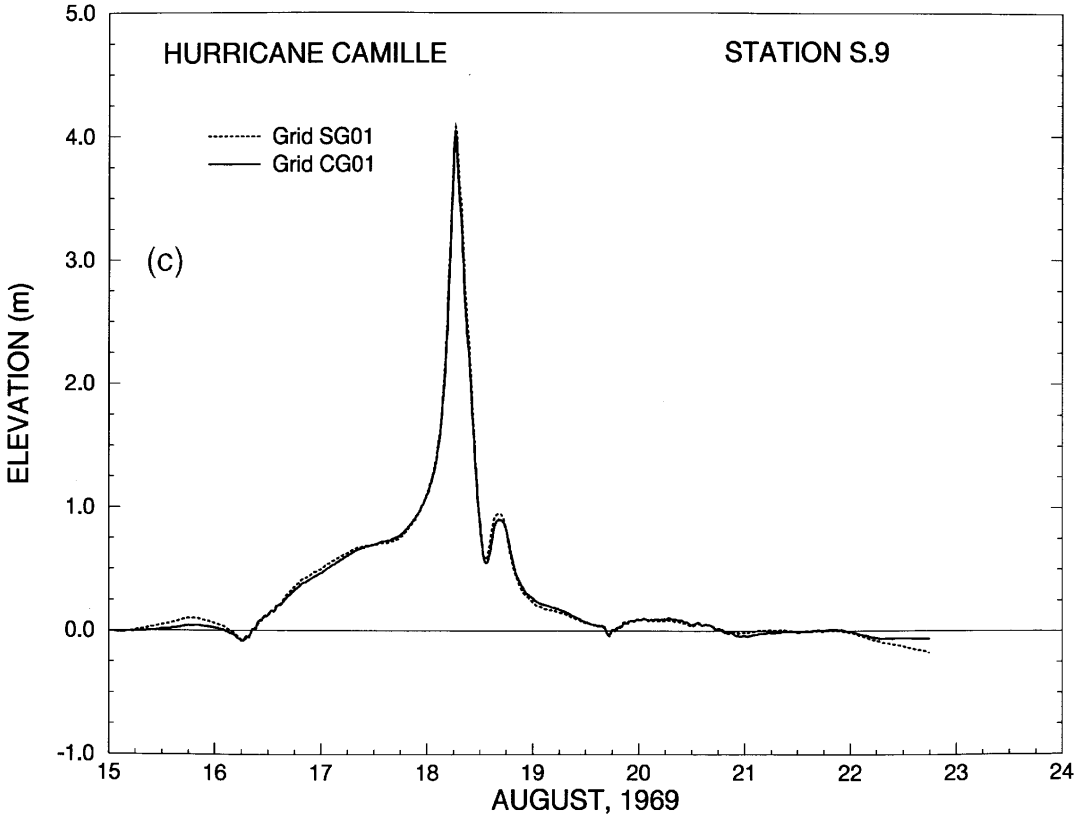

Figure 14. (*contined*)

Biloxi, Mississippi will reduce the level of the extreme overprediction error which coincides with the peak surge as the hurricane makes landfall.

6. CONCLUSIONS

Discretization of the computational domain can significantly affect the computed storm surge elevations throughout the domain. Over deep water, insufficient grid resolution leads to sizable underprediction errors. Smearing or damping of the inverted barometer forcing function, a consequence of interpolating the pressure forcing function onto a grid of discrete points, causes the peak inverted barometer effect in the storm surge to be underpredicted. Theoretical interpolation errors associated with the inverted barometer forcing function are well correlated to the normalized errors computed in the grid convergence study.

Over shallower waters on the continental shelf, underresolution of the grid leads to dominant overprediction errors and an overpredicted peak surge at the coast. All simulations in the grid convergence study indicate that near-coastal resolution is the most critical factor for accuracy of storm surge computations. Despite variation of the hurricane path, spatial scale and forward velocity, refinement of the coastline and resolution in coastal regions remain the primary factors affecting hurricane storm surge predictions in relation to the grid discretization. Furthermore, it is observed that complexity of the shoreline causes dramatic increases in storm surge which, in turn, are accompanied

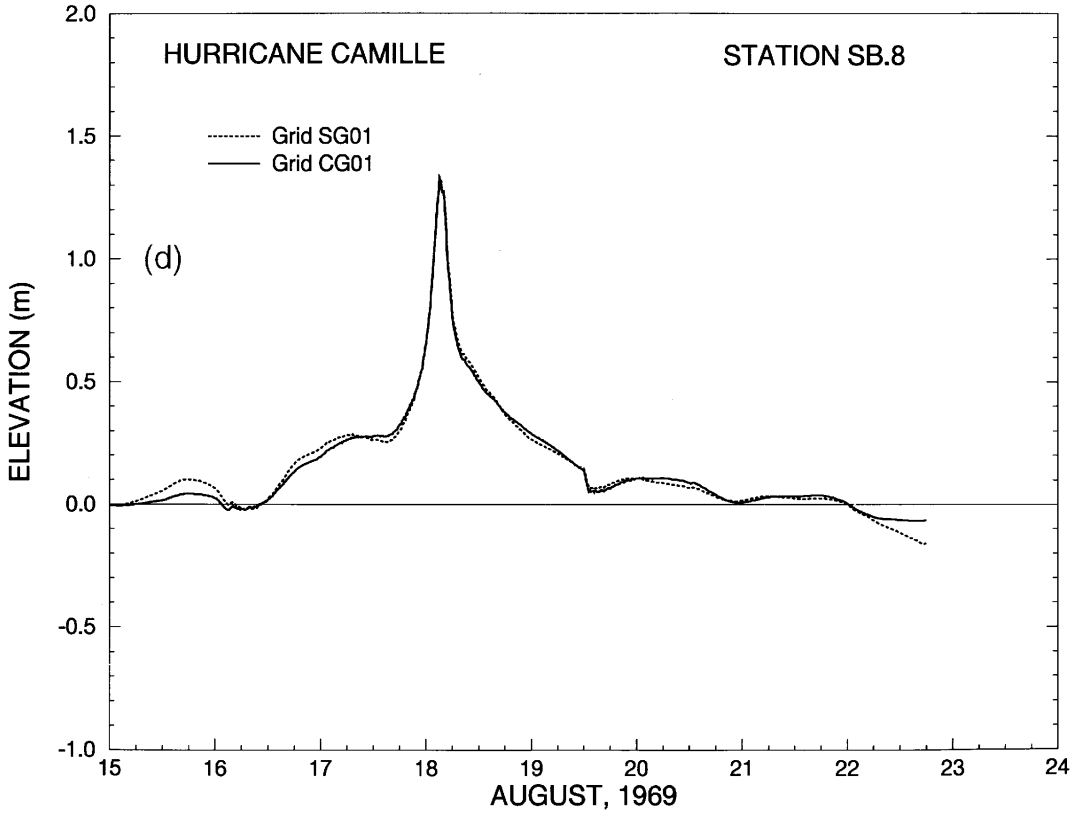

Figure 14. (*contined*)

by increased extreme errors in underresolved regions. Normalized errors are essentially unaffected by the spatial variability of the coastline.

The analyses herein demonstrate general trends in the storm surge prediction errors relative to the spatial discretization and suggest a gridding strategy to address these errors. Determination of the exact grid spacing required in coastal areas depends primarily on the complexity of the coastline detail and the extent of very shallow waters. Error analysis and a grid convergence study such as that presented are necessary so that resolution requirements may be evaluated on a case-by-case basis.

The disparity between grid resolution requirements in the deep ocean and coastal regions suggests that a graded grid structure is most appropriate. The variation in nodal density arises from the significant refinement necessary in shallow coastal areas where storm surge generation is important and coastline detail and/or bathymetric change can be complex in conjunction with the coarse discretizations over the deep ocean where processes occur more gradually and are of less interest. Though discretization errors can never be completely eliminated, errors associated with the variably graded grids used here are relatively uniform throughout the storm simulation. In addition to providing uniform errors, the variable grid structure minimizes computational effort, an important consideration when implemented in conjunction with large domains. The flexibility of the finite element approach used to discretize the grids within this study leads to easy incorporation of coastline detail and nodal densities which range over several orders of magnitude. Implementation of a graded grid discretization over large domains coupled with the efficiency of the finite element method leads

to a discrete problem that remains well within computational limits. Application of this variably graded discretization strategy to the simulation of storm surge generated by Hurricane Camille leads to errors in predicted storm surge that remain fairly uniform for the duration of the storm. This uniformity of the error is essential to minimizing the influence of the spatial discretization on storm surge computations.

Grid convergence studies similar to those presented should always be conducted to assess performance of any grid. In this way, numerical errors resulting from the grid discretization can be identified and distinguished from the computed physics. Grid convergence studies are the pathway to obtaining a grid discretization which is both computationally efficient and results in accurate predictions of hurricane storm surge in coastal regions.

ACKNOWLEDGEMENTS

This research was supported by the U.S. Army Engineer Waterways Experiment Station under contracts DACW-39-90-K-0021 and DACW-39-95-K-0011 and by the National Science Foundation under grant OCE-9116448. We thank Dr. A. M. Baptisa of the Oregon Graduate Institute for allowing us to use the grid generation and visualization software packages XMGREDIT and XMVIS. This paper, NRL contribution PP-7322-96-0011 is approved for public release; distribution unlimited.

REFERENCES

1. B. Johns, S. K. Dube, U. C. Mohanty and A. D. Rao, 'Simulation of storm surges using a three-dimensional numerical model: an application to the 1977 Andhra Cyclone', *Q. J. R. Meteorol. Soc.*, **109**, 211–224 (1983).
2. B. Johns, S. K. Dube, U. C. Mohanty and A. D. Rao, 'On the effect of bathymetry in numerical storm surge simulation experiments', *Comput. Fluids*, **11**, 161–174 (1983).
3. C. Le Provost and P. Vincent, 'Some tests of precision for a finite element model of ocean tides', *J. Comput. Phys.*, **65**, 273–291 (1986).
4. J. R. Bennett and J. E. Campbell, 'Accuracy of a finite-difference method for computing lake currents', *J. Comput. Phys.*, **68**, 262–271 (1987).
5. D. E. Dietrich, P. J. Roache and M. G. Marietta, 'Convergence studies with the Sandia Ocean Modeling System', *Int. j. numer meth. fluids*, **11**, 127–150 (1990).
6. J. J. Westerink and W. G. Gray, 'Progress in surface water modeling', *Rev. Geophys.*, **29**, April suppl., 210–217 (1991).
7. R. W. Lardner and Y. Song, 'A comparison of spatial grids for numerical modelling of flows in near-coastal seas', *Int. j. numer. meth. fluids*, **14**, 109–114 (1992).
8. S. Piacsek and R. Allard, 'The importance of horizontal resolution in coupled ice/ocean models of the Arctic', *Presented at SIAM Conf. on Mathematical and Computational Issues in the Geosciences*, Houston, TX, April 1993.
9. D. E. Dietrich, 'A numerical study of small scale continental shelf features and their interactions with deep water flows', *Presented at SIAM Conf. on Mathematical and Computational Issues in the Geosciences*, Houston, TX, April 1993.
10. D. E. Dietrich, 'On modeling geophysical flows having low Rossby numbers', *Atmosphere–Ocean*, **31**, 57–71 (1993).
11. J. J. Westerink, R. A. Luettich and J. C. Muccino, 'Modeling tides in the western North Atlantic using unstructured graded grids', *Tellus*, **46A**, 187–199 (1994).
12. J. J. Westerink, R. A. Luettich, C. A. Blain and S. C. Hagen, 'The utility of the finite element method in computing surface elevation and circulation in continental margin waters', in G. F. Carey (ed) *Finite Element Modeling of Environmental Problems*, Wiley, Chichester, 1994.
13. R. A. Luettich and J. J. Westerink, 'Continental shelf scale convergence studies with a barotropica tidal model', in D. R. Lynch and A. M. Davies (eds), *Quantitative Skill Assessment for Coastal Ocean Models*, AGU Press, Washington, DC, 1995.
14. R. A. Flather, 'A numerical model investigation of the storm surge of 31 January and 1 February 1953 in the North Sea', *Q. J. R. Meteorol. Soc.*, **110**, 591–612 (1984).
15. S. A. Dendrou, C. I. Moore and V. A. Myers, 'Application of storm surge modeling to coastal flood rate determinations', *Marine Sci. Technol. J.*, **19**, 42–49 (1985).
16. S. K. Dube, P. C. Sinha and G. D. Roy, 'Numerical simulation of storm surges in Bangladesh using a bay–river model', *Coastal Engng.*, **10**, (1986).
17. J. J. Westerink, K. D. Stolzenbach and J. J. Connor, 'General spectral computations of the nonlinear shallow water tidal interactions within the Bight of Abaco, *J. Phys. Oceanogr.*, **19**, 1350–1373 (1989).

18. A. H. Al-Rabeh, N. Eunay and H. M. Cekirge, 'A hydrodynamic model for wind driven and tidal circulation in the Arabian Gulf', *Appl. Math. Model.*, **14**, 410–419 (1990).
19. G. D. Hubbert, L. M. Leslie and M. J. Manton. 'A storm surge model for the Australian Region', *Q. J. R. Meteorol. Soc.*, **116**, 1005–1020 (1990)
20. J. J. Westerink, R. A. Luettich and S. C. Hagen, 'Meshing requirements for large scale coastal ocean tidal models', in A. Peters, G. Wittum, B. Herrling and U. Meissner (eds), *Numerical Methods in Water Resources*, Kluwer, Dordrecht, 1994.
21. C. A. Blain, 'The influence of domain size and grid structure on the response characteristics of a hurricane storm surge model', *Ph.D. Dissertation*, Department of Civil Engineering and Geological Sciences, University of Notre Dame, Notre Dame, IN, 1994.
22. C. A. Blain, J. J. Westerink and R. A. Luettich, 'Domain and grid sensitivity studies for hurricane storm surge predictions', in A. Peters, G. Wittum, B. Herrling and U. Meissner (eds), *Numerical Methods in Water Resources*, Kluwer, Dordrecht, 1994.
23. C. A. Blain, J. J. Westerink and R. A. Luettich Jr., 'The influence of domain size on the response characteristics of a hurricane storm surge model', *J. Geophys. Res.*, **99** (C9), 18,467–18,479 (1994).
24. P. J. Roache, 'Perspective: a method for uniform reporting of grid refinement studies', *J. Fluids Engng.*, **116**, 405–413 (1994).
25. R. A. Luettich, J. J. Westerink and N. W. Scheffner, 'ADCIRC: an advanced three-dimensional circulation model for shelves, coasts and estuaries, Report 1: Theory and methodology of ADCIRC-2DDI and ADCIRC-3DL', *Tech. Rep. DRP-92-6*, Department of the Army, 1992.
26. R. L. Kolar, W. G. Gray, J. J. Westerink and R. A. Luettich, 'Shallow water modeling in spherical coordinates: equation formulation, numerical implementation, and application', *J. Hydraul. Res.*, **32**, 3–24 (1994).
27. D. R. Lynch and W. G. Gray, 'A wave equation model for finite element tidal computations', *Comput. Fluids*, **7**, 207–228 (1979).
28. D. R. Lynch, 'Progress in hydrodynamic modeling, review of U.S. contributions, 1979–1982', *Rev. Geophys. Space Phys.*, **21**, 741–754 (1983).
29. I. P. E. Kinnmark, 'The shallow water wave equations: formulation, analysis and application', *Ph.D. Dissertation*, Department of Civil Engineering, Princeton University, 1984.
30. R. L. Kolar, J. J. Westerink, M. E. Cantekin and C. A. Blain, 'Aspects of nonlinear simulations using shallow water models based on the wave continuity equation', *Comput. Fluids*, **23**, 523–538 (1994).
31. V. J. Cardone, C. V. Greenwood and J. A. Greenwood, 'Unified program for the specification of hurricane boundary layer winds over surfaces of specified roughness', *CR-CERC-92-1*, Coastal Engineering Research Center, U.S. Army Engineers, 1992.
32. C. P. Jelesnianski and A. D. Taylor, 'A preliminary view of storm surges beofre and after storm modifications', *NOAA Tech. Memo. ERL WMPO-3*, 1973.
33. J. R. Garratt, 'Review of drag coefficients over oceans and continents', *Mon. Wea. Rev.*, **105**, 915–929, 1977.
34. M. R. Bunpapong, R. O. Reid and R. E. Whitaker, 'An investigation of hurricane-induced forrerunner surge in the Gulf of Mexico', *Tech. Rep. CERC-85-5*, Coastal Engineering Research Center, U.S. Army Engineers, 1985.
35. J. J. Westerink and P. Roache, 'Issues in convergence studies in geophysical flow computations', in G. Delic and M. Wheeler (eds), *Next Generation Environmental Models Computational Methods*, SIAM, Philadelphia, PA, 1996.
36. B. R. Jarvinen, C. J. Neumann and M. A. S. Davis, 'A tropical cycline data tape for the North Atlantic Basin, 1886–1992', *NOAA Data Tape*, 1993.

